Comprehensive Power Flow Analyses and Novel Feedforward Coordination Control Strategy for MMC-Based UPFC

Jinlian Liu *[ID], **Zheng Xu**[ID] **and Liang Xiao**[ID]

College of Electrical Engineering, Zhejiang University, Hangzhou 310027, China; xuzheng007@zju.edu.cn (Z.X.); xlxiaoliang@zju.edu.cn (L.X.)
* Correspondence: ljl0323@zju.edu.cn; Tel.: +86-571-8795-2074

check for updates

Abstract: This paper aims to discover the general steady-state operation characteristics, as well as improving the dynamic performance, of the modular multilevel converter (MMC)-based unified power flow controller (UPFC). To achieve this, first, we established a detailed power flow model for MMC-based UPFC containing each critical part and made qualitative and graphical analyses combining 2-dimensional operation planes and 3-dimensional spatial curve surfaces comprehensively to derive general power flow principles and offer necessary references for regulating UPFC. Furthermore, to achieve better performance, we designed a feedforward control strategy for the shunt and series converters of UPFC, both comprising two feedforward control blocks with the introduction of necessary compensating branches, and analyzed the performance in complex and time domain, respectively. The proposed power flow principles and control strategies were validated by a (power systems computer aided design) PSCAD model of 220 kV double-end system; the results reveal the MMC-based UPFC can realize the power flow principles and improve the control speed, stability, and precision of the power flow regulations under various conditions.

Keywords: MMC-based UPFC; detailed power flow model; 2-dimensional operation planes; 3-dimensional spatial curve surfaces; feedforward coordination control strategy

1. Introduction

To improve the transfer capacity and controllability of modern power systems, insulated gate bipolar translator (IGBT)-based (flexible AC transmission systems) FACTS devices are widely used. For examples, the static synchronous compensators (STATCOM) are used as shunt controllers and the static synchronous series compensators (SSSC) are serving as series controllers. Among all the FACTS devices, the most universal is the unified power flow controller (UPFC), which combines the shunt and series controller together [1–5].

As an advanced and multi-functional utility, UPFC possesses all the requisite functions of the voltage regulation, phase shifting, and impedance compensation and comprehensive governing, to regulate the real and reactive power of the transmission lines simultaneously and quickly, improving the transfer flexibility capability and stability of the power grids [6,7]. In recent years, with the emerging concept and technology of MMC [8–10], which has been known the most prospective and practicable (voltage source converter) VSC devices in manufacture and engineering, the MMC-based UPFC have also been proposed and implemented in practice, of which the two leading projects are the 220kV UPFC demonstration project in Nanjing western grid and the UPFC project on the 500 kV power grid in southern Suzhou, both have been tested effective to regulate power flows quickly and precisely, also have the ability to eliminate the overload of key transmission sections under worse

contingencies [11–13]. For the priority of MMC-based UPFC in high-voltage grids, this paper will also adopt the MMC-based UPFC in modeling and simulation.

In recent years, a certain amount of research regarding mathematical models and power flow analyses of UPFC has been carried out. Reference [14] derived the state space equations of UPFC in stationary and rotating orthogonal coordinate system, respectively. The authors in [15] built an improved steady-state mathematical model based on injected powers considering the operational losses. Reference [16] summarized varieties of UPFC static models in power flow algorithm, such as load injection model, decoupled model, π load injection model, indirect model, and so on. In [17], the authors proposed a current-based model and compared its performance with the power injection model in power flow evaluations through a Quasi-Newton optimization approach. The authors in [18] developed a new power frequency model of UPFC which is appropriate for system dynamic behavior and calculate the interface of UPFC to the ac grid with reduced bus admittance matrix. A new static model of the UPFC was investigated in [19], which was incorporated into the modified standard load flow programs without basically changing the programs to study the load flow problem of a power system.

However, details concerning each critical part along the transmission line are omitted in the above power flow models of UPFC. In addition, the power flow analyses are based on complex math expressions, which reduce the applicability and practicability to a significant extent. Also, the corresponding analyses almost concentrated on a whole and abstract viewpoint, resulting in that it is difficult for the dispatchers to figure out the power flow principles intuitionally and quickly, and to offer figurate and qualitative control references to regulate the UPFC and ac grids merely through visualized estimation.

Research on the control strategy of UPFC has never stopped in recent years. References [20–23] researched the cross-coupling scheme to control UPFC, by which the real and reactive power will affect each other obviously when regulating one individually. Reference [24–26] developed the decoupled controlled strategy of UPFC, which yields the controlled d-axis and q-axis current component through a derived current calculator. This method improved the response speed of the system to power flow changes but is still limited to eliminate the dynamic interaction between the real and reactive power flow through the transmission line. The authors in [27] also researched a coordination control strategy of UPFC, which brought feedforward quantities into the shunt converter control scheme, achieving better dynamic response performance, but had no effect on modifying the real power flow. References [28,29] also proposed the active and reactive power flow coordination control strategy based on PI approach. There are also some other advanced control methods for UPFC based on Lyapunov direct method, line loss minimization, fuzzy logic controller, sliding mode controller and so on [30–33].

Nevertheless, on the one hand, some of these control methods above have comparably complex structures and principles, which are difficult to be implemented in engineering. On the other hand, some other methods might have not been considerate in the performance of accuracy, response speed, and stability of controlling UPFC. Therefore, these methods have not taken the applicability of structure and performance of control into consideration at the same time, so it is still necessary to search for better control methods which can realize the above control targets to a larger extent, with a comparably simple structure.

This paper mainly contributes to the following aspects. On the one hand, in order to illustrate the power flow principles of the UPFC intuitionally, and offer applicable and practical regulation references for controlling UPFC through qualitative estimation, we establish the detailed power flow model of MMC-based UPFC considering each critical part of the line and analyze the principles combining 2-dimensional power operation plane and 3-dimension spatial power operation surfaces under various typical conditions, respectively.

On the other hand, for the sake of improving the control effect on response speed, stability, and accuracy for UPFC, also being easy to implement and practice, we design a novel feedforward

coordination control strategy which comprises of basic inner-loops and outer feedforward control blocks for both the shunt and series converters, the feedforward blocks provide requisite references with the introduction of necessary compensating branches for the input components of the inner-loops through derivation, thus realizing more reasonable and accurate control performance.

This paper consists of the following sections. Firstly, we introduce the UPFC embedded double-end power system and MMC structures in Section 1. Then, we derive out the detailed power flow models of UPFC and make analyses under various typical conditions combining plane and spatial viewpoints. In Section 3, the inner-loops and feedforward blocks of the control schemes for both the shunt and series converter are designed out, which are analyzed in complex and time domain, respectively. In Section 4, we validate the power flow principles and control strategy by numeric simulation. The conclusions were summarized in the last section.

2. Structure of MMC-based UPFC

The MMC-based UPFC is mainly composed of two back-to-back MMC converters interconnected by a DC voltage link, the structure of which embedded in a two-end system is as shown in Figure 1. In the diagram, V_s and V_r stand for the sending end and receiving end voltage source, I_s and I_r stand for the corresponding current, V_1 and V_2 are the voltage of shunt side bus 1 and series side bus 2 of UPFC. I_{sh} and I_{se} are the exit current the shunt converter and series converter. I_1 is the current from bus 1 to bus 2. v_{12} represents the series embedded voltage of UPFC. For convenience, C_{eq} is assumed as the dc side equivalent capacitance of the MMC, which does not exist in the real application. I_{dc1}, I_{dc2}, I_{dc}, and I_{loss} describe for dc side current of shunt and series converter, the current through C_{eq}, and the dc side loss current, respectively. Z_s, Z_r, Z_{sh}, and Z_{se} are the sending end impendence, the receiving end impendence, the ac side impendence of shunt and series converter, respectively. The phasor diagram of UPFC is also displayed in Figure 1.

(**a**)   (**b**)
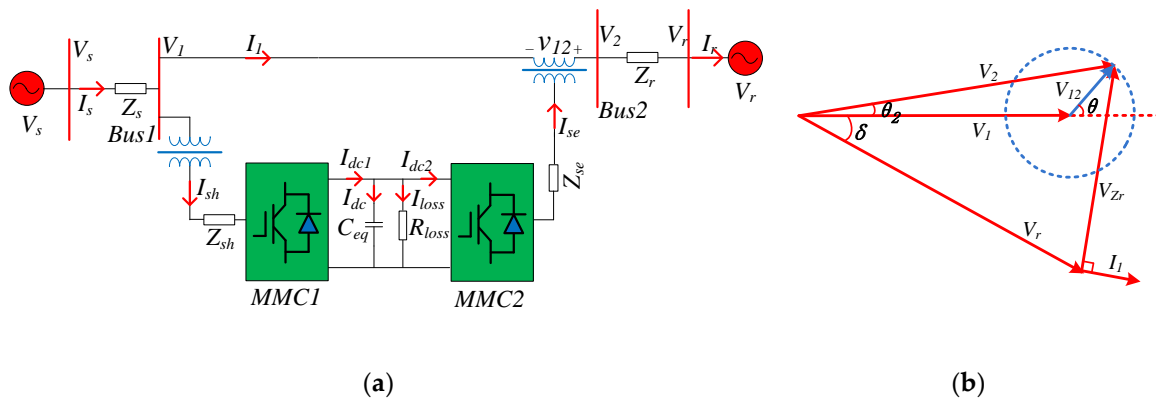
Figure 1. Schematic diagrams of MMC-based UPFC: (**a**) Structural diagram of MMC-based UPFC; (**b**) Phasor diagram of the parameters of UPFC.

The structure diagram of MMC with its submodule is depicted in Figure 2. In the diagram, we assume that there exist 2N submodules in each phase bridge, with average N modules distributed in the upper or lower bridge. i_{pj} and i_{nj} stands for the one phase current through the upper and lower bridge arm, i_{vj} and represents the output current of ac side, and i_{diffj} means the internal circulating current of one phase circuit. Thus, we can have the following expressions,

$$\begin{cases} i_{pj} = i_{vj}/2 + i_{diffj} \\ i_{nj} = -i_{vj}/2 + i_{diffj}(j = a, b, c) \\ i_{diffj} = (i_{pj} + i_{nj})/2 \end{cases} \tag{1}$$

Based on the Kirchhoff's laws, the following math models can be deduced,

$$
\begin{cases}
R_0 i_{diffj} + L_0 di_{diffj}/dt = u_{dc}/2 - (u_{nj} + u_{pj})/2 \\
u_{vj} = (u_{nj} - u_{pj})/2 - (R_0 i_{vj} + L_0 di_{vj}/dt)/2 \\
u_{sj} = u_{vj} - (R_s i_{vj} + L_s di_{vj}/dt)
\end{cases}
\tag{2}
$$

Here, it is assumed that the variable $e_j = (u_{nj} - u_{pj})/2$ stands for the inner differential-mode voltage of single-phase bridge arm, $e_{comj} = (u_{nj} + u_{pj})/2$ represents the inner common-mode voltage, $R_m = (R_s + R_0/2)$ and $L_m = (L_s + L_0/2)$ stand for the equivalent resistance and conductance of single-phase respectively, and $u_{diffj} = R_0 i_{diffj} + L_0 di_{diffj}/dt$ represents the inner-loop imbalance voltage of one phase. Then we will get the following equation,

$$
u_{sj} = e_j - (R_m i_{vj} + L_m di_{vj}/dt)
\tag{3}
$$

In addition, with the energy balance of the capacitor storage, we can obtain the equation like,

$$
1/2 C_{eq} U_{dc}^2 = 3 \cdot (2N) \cdot (1/2 C_{sm} U_{sm}^2)
\tag{4}
$$

From the MMC structure, we can have the relation $U_{dc} = N \cdot U_{sm}$, substitute it into the above equation, the equivalent capacitance of the dc side of MMC can be obtained as follows,

$$
C_{eq} = (6/N) C_{sm}
\tag{5}
$$

The modulation method of MMC usually adopts the Nearest Level Modulation (NLM), which is more adaptive under larger electric levels conditions. The corresponding voltage modulation ratio is defined as $m_v = e_j/(u_{dc}/2)$, and the current modulation ratio is $m_I = (I_v/2)/(I_{dc}/3)$.
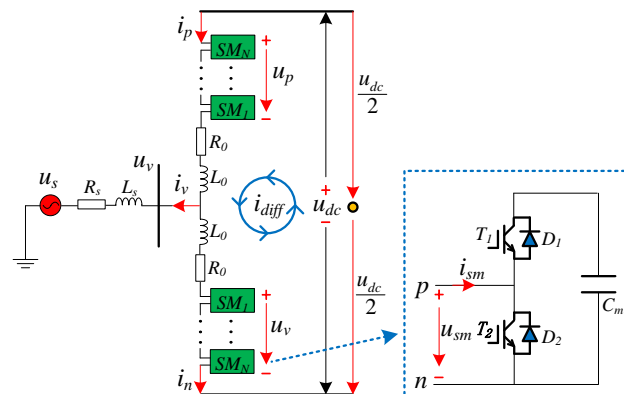
Figure 2. Structural diagram of MMC on inverter side and its submodule (SM).

3. The Detailed Power Flow Model and Analyses of UPFC

3.1. Detailed Power Flow Model of UPFC

First of all, from the diagram in Figure 1, the shunt side bus 1 V_1, the series embedded voltage v_{12}, the series side bus 2 V_2, the receiving end bus Vr and the impendence Z_r of receiving end are assumed as the five critical parts of power flow along the transmission line, and we will derive the detailed power flow model of each critical part in the following.

The initial parameters are assumed as, $\dot{V}_1 = V_1 \angle 0$, $\dot{V}_s = V_s \angle \theta_s$, $\dot{V}_{12} = V_{12} \angle \theta$, $\dot{V}_2 = V_2 \angle \theta_2$, $\dot{V}_r = V_r \angle \delta$, $\dot{I}_1 = I_1 \angle \theta_1$, $\dot{V}_2 = \dot{V}_1 + \dot{V}_{12} = (V_1 + V_{12} \cos \theta) + jV_{12} \sin \theta$, $Z_r = R_r + j\omega L_r$, $\dot{V}_r = \dot{V}_2 - \dot{I}_1 Z_r$, $\dot{I}_1 = (\dot{V}_2 - \dot{V}_r)/Z_r$.

To obtain the simple structure of power flow equations, it is necessary to replace some expressions with specified substitutions, they are set as, $m = V_1 + V_{12}\cos\theta - V_r\cos\delta$, $n = V_{12}\sin\theta - V_r\sin\delta$, $Z_r^2 = R_r^2 + (\omega L_r)^2$, $a = V_r\cos\delta$, $b = V_r\sin\delta$, $c = V_{12}\cos\delta$, $d = V_{12}\sin\delta$.

Based on the structure diagram, the power flow directions of all parts have been uniformly set in sending out direction, except for the power flow through receiving end impendence, which are in absorbing direction.

The shunt side bus 1 power is calculated by the following formulas,

$$\begin{cases} P_1 = real(\dot{V}_1 \cdot \dot{I}_1^*) = (R_r m + \omega L_r n)V_1/Z_r^2 \\ Q_1 = imag(\dot{V}_1 \cdot \dot{I}_1^*) = (R_r n - \omega L_r m)V_1/Z_r^2 \end{cases} \tag{6}$$

The power injected into the ac grid by the series transformer of UPFC are represented below,

$$\begin{cases} P_{12} = real(\dot{V}_{12} \cdot \dot{I}_1^*) = [R_r(cm + dn) + \omega L_r(cn - dm)]/Z_r^2 \\ Q_{12} = imag(\dot{V}_{12} \cdot \dot{I}_1^*) = [R_r(cn - dm) - \omega L_r(cm + dn)]/Z_r^2 \end{cases} \tag{7}$$

In addition, the power flow through the series side bus 2 are displayed as below,

$$\begin{cases} P_2 = real(\dot{V}_2 \cdot \dot{I}_1^*) = [R_r(V_1 m + cm + dn) + \omega L_r(V_1 n + cn - dm)]/Z_r^2 \\ Q_2 = imag(\dot{V}_2 \cdot \dot{I}_1^*) = [R_r(V_1 n + cn - dm) - \omega L_r(V_1 m + cm + dn)]/Z_r^2 \end{cases} \tag{8}$$

The power flow through the receiving end impendence Z_r are deduced as follows,

$$\begin{cases} P_{Z_r} = real(\dot{V}_{Z_r} \cdot \dot{I}_1^*) = R_r(m^2 + n^2)/Z_r^2 \\ Q_{Z_r} = imag(\dot{V}_{Z_r} \cdot \dot{I}_1^*) = \omega L_r(m^2 + n^2)/Z_r^2 \end{cases} \tag{9}$$

Finally, the receiving end power are listed as follows,

$$\begin{cases} P_r = real(\dot{V}_r \cdot \dot{I}_1^*) = [R_r(am + bn) + \omega L_r(an - bm)]/Z_r^2 \\ Q_r = imag(\dot{V}_r \cdot \dot{I}_1^*) = -[R_r(an - bm) + \omega L_r(am + bn)]/Z_r^2 \end{cases} \tag{10}$$

In the equations above, all of them are with the magnitude a phase of v_{12} as independent variables, revealing that the power flow of each parts along the lines are mainly regulated by the series embedded voltage of UPFC.

3.2. Power Flow Analyses in Plane and Spatial Domain

To analyze the general power flow principles of each key part along the line intuitively and qualitatively, and acquire the necessary references or rules to regulate the UPFC more indicatively and orientated. In this section, we will carry out the power flow analyses through 2-dimensional operation planes and 3-dimensional spatial operation curve surfaces based on the math models above, respectively.

To reflect the general conditions, we choose $v_r = 1$, $\delta = -\pi/8$ as the normal condition, the primary parameters of the system are assumed as $\dot{V}_1 = 1\angle 0\ p.u.$, $\dot{V}_r = 1\angle(-\pi/8)\ p.u.$, $R_r = 0.025\ p.u.$, $\omega L_r = 0.5\ p.u.$, $L_{sh} = L_{se} = 2$ mH, $R_{sh} = R_{se} = 0.05\ \Omega$, $R_{loss} = 0.5\ \Omega$.

As is known, the UPFC mainly control the power flows by the magnitude and phase of series embedded voltage v_{12}. Thus, it is reasonable to choose the magnitude and phase θ of v_{12} as the independent variables, here it is assumed that the magnitude of v_{12} ranges from 0 p.u. to 0.18 p.u. with a 0.01 step, and the phase difference δ varies from $-\pi$ to π.

To take the normal and worse conditions of the system into consideration, here, we assume several typical conditions to reflect the power flow principles comprehensively, which have been listed in Table 1.

Table 1. The typical conditions set in power flow analyses.

Conditions	Voltage Magnitude V_r	Phase δ
Normal condition 1	1	$-\pi/8$
Varying condition 2	1	$-\pi/24$
Varying condition 3	0.9	$-\pi/8$
Varying condition 4	1.1	$-\pi/8$
The worst condition 5	0.82	$-\pi/2$

3.2.1. Power Flow Analyses Under Normal Condition 1

First, we will figure out the pictures concerning the reactive power against the real power under normal condition from the viewpoint of the 2-dimensional operation planes.

It can be seen in Figure 3 that when the magnitude v_{12} fixes at a certain value, both the traces of real power and reactive power of each part all moves along one elliptical closed-loop within certain ranges, meaning the real power and the reactive power of each part are varying and restricting each other mutually. The only exception is that the active power and reactive power losses on the receiving end impendence of P_{zr} and Q_{zr} are changing linearly, of which the slope is just the ratio of X_r and R_r.
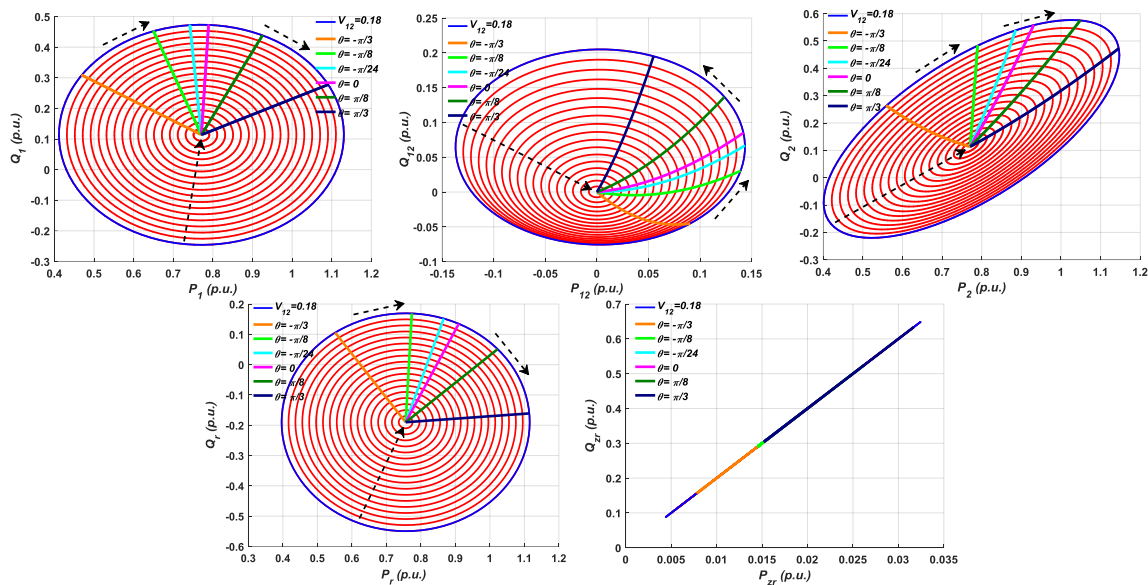
Figure 3. The 2-dimensional power flow operation planes of each part when $V_r = 1$, $\delta = -\pi/8$.

We can also see all the elliptical traces of power flow will contract inwardly until decreasing to zero when the magnitude of v_{12} decrease from 0.18 p.u. to 0 with 0.01 decrement, revealing that the magnitude of v_{12} dominantly determines the operation ranges and area of the power flows. Please note that the areas of the closed ellipses stand for the power flow capacity of each part, and the capacity of v_{12} may be the smallest among all the parts, which may indicate that we can use limited capacity of v_{12} to control much larger capacity of the system. Moreover, the elliptical traces of lower region are denser to some extents among different loops, than those of the upper region. The reason may be that when v_{12} absorbs reactive power from the ac grid, part of the reactive power must be applied for the excitation power needed by the series transformer, resulting in certain losses. It should also be noted that the traces of P_2—Q_2 present longer in the horizontal axis, implying the UPFC has significantly impacted the real power through the series side bus$_2$ that the varying rate of P_2 is larger than others.

Furthermore, if we choose a list of typical phase θ as $-\pi/3$, $-\pi/8$, $-\pi/24$, 0, $\pi/8$ and $\pi/3$, it can be seen the power flow traces of v_{12} moves in the counterclockwise direction along the elliptical traces while that of the other parts move inversely, which may imply that the power flow principles of v_{12} may have significant difference to the others, and it may be necessary to adopt much different

control method for the components of v_{12} from other parts, so that the system can be regulated feasibly by the UPFC.

To acquire the power flow operation principle entirely, we also analyzed the principles of power flows against the phase θ of v_{12} from another plane viewpoint.

Above all, Figure 4 also display the results under the normal condition, the power flows of each part against phase θ appear as certain sinusoidal waveforms with different magnitudes and initial phases, and the same as before, the magnitudes of the curves are all proportional to the magnitudes of v_{12}, among which the middle lines where $v_{12} = 0$ means the original power flow without UPFC embedded. Please note that all the curves of each part are much denser in the sections of θ riding through the middle line, which coincide with Figure 3 as expected.
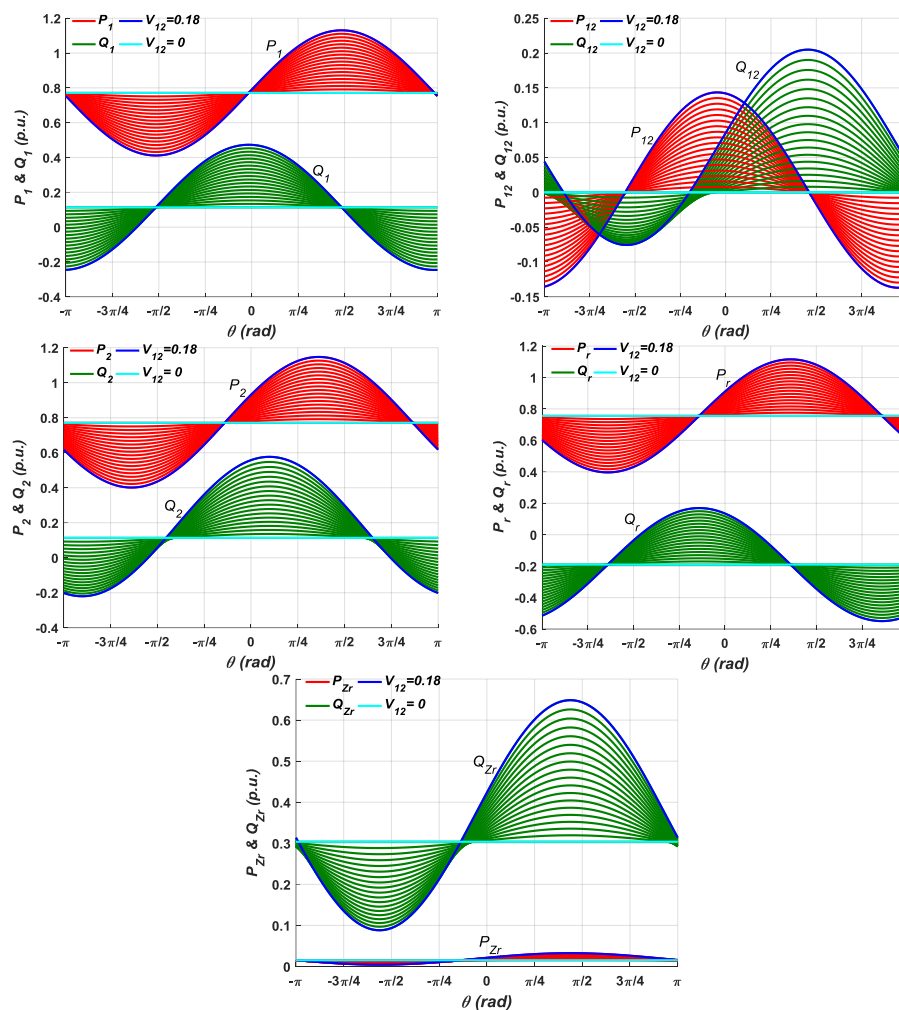
Figure 4. The 2-dimensional power flow planes against phase θ of each part when $V_r = 1$, $\delta = -\pi/8$.

It can be seen similarly as before that the area of the power flow curves of v_{12} are still the smallest, and the ranges and areas of the lower half regions of the curves are apparently smaller than the upper half regions because of the compensation for the excitation power, while the other parts of the line have nearly symmetrical curves between the upper and lower regions.

Note also that the real and reactive power curves of v_{12} intersect mutually in several sections of θ, but those of the other parts along the line have hardly any intersections. This may reveal that there exist more than one forms of v_{12} regarding one power flow point within certain sections of θ. In contrast, there may be only one form of v_{12} regarding one power flow point for other parts of the line. This phenomenon implies that within the intersections regarding phase θ, the system may become more intense oscillating and contain more harmonics.

Therefore, it is not reasonable to regulate the power flow of the line directly by the power flow of v_{12}, but by other variables. The results also validate the power flow principles of v_{12} analyzed as above.

After discussing the power flow principles in the plane, we will continue to analyze the power flow principles in 3-dimensional spatial operation curve surfaces, which will display the power flow principles from another viewpoint.

First, Figure 5 also depicts the power flow operation curve surfaces under normal condition. It can be seen the surfaces of each part appears as one kind of approximate conical shapes except those of the receiving end impendence. The top loops of the surfaces stand for the traces of v_{12} = 0.18 p.u., the loop will also contract inwardly by step along with 0.01 p.u. decrement until the zero vertexes. Therefore, the area of the power flow surface can represent the capacity of power flow graphically, and the variation of the surface shapes may also indicate the changing rules of power flow.
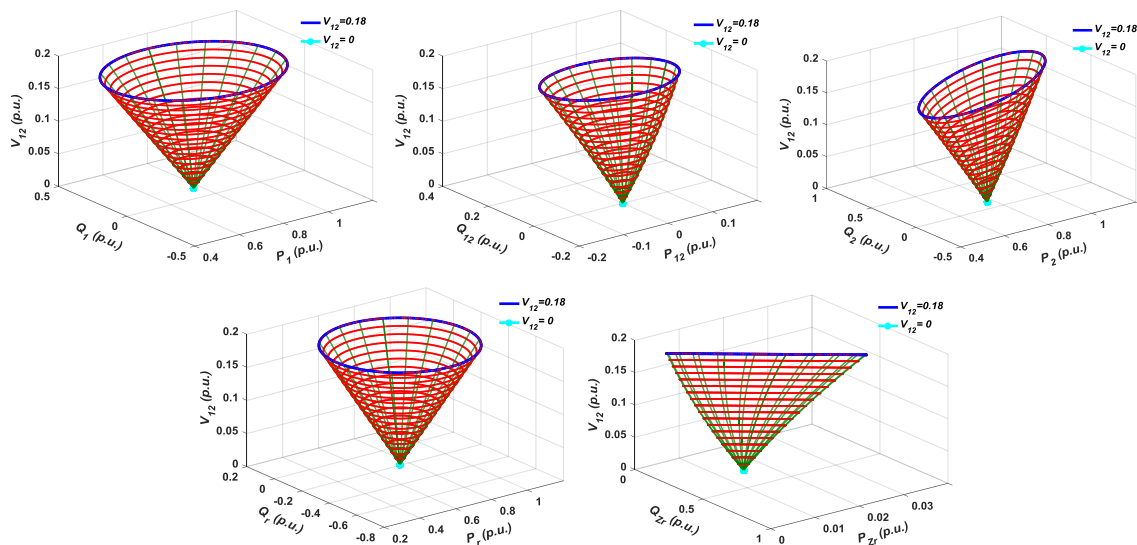
Figure 5. The spatial power flow operation surfaces when $V_r = 1$, $\delta = -\pi/8$.

It can be seen the area of the surface of v_{12} is also the smallest, and those of the other parts along the line all have different shapes and area. The results also accord with the analyses in the planes above.

3.2.2. Power Flow Analyses under Varying Condition 2

To understand the power flow principles of the system in other cases, next, we will consider the conditions when $V_r = 1$ and phase $\delta = -\pi/24$. All kinds of figures of the results have been listed in Figure 6, it can be viewed that the shape of the spatial operation surfaces of v_{12} have obviously inclined and bent to some degree, the resulting area of the surfaces may also have much reduced, meaning the regulating capabilities of UPFC have descended apparently. We can also see the intersections of real and reactive power of v_{12} turn out to be much larger and concentrated within certain sections of θ, the results may imply more intense fluctuations and higher Total Harmonic Distortion (THD) of power quality during the regulations of UPFC, the stability and power quality of the system may have deteriorated to some extent.

Moreover, the difference between the upper and the lower half region of reactive power of v_{12} have become much larger that the lower half region has almost shrunk to a very little value, leading that the capability of absorbing reactive power of UPFC may have become very weak, namely, the reactive power support of the receiving end may become weaker under this condition.

In contrast, the shapes of the spatial surfaces of the other part have not changed much, but only the areas of those have decreased a little, validating the UPFC can still efficiently regulate the power flows of the system under this condition.
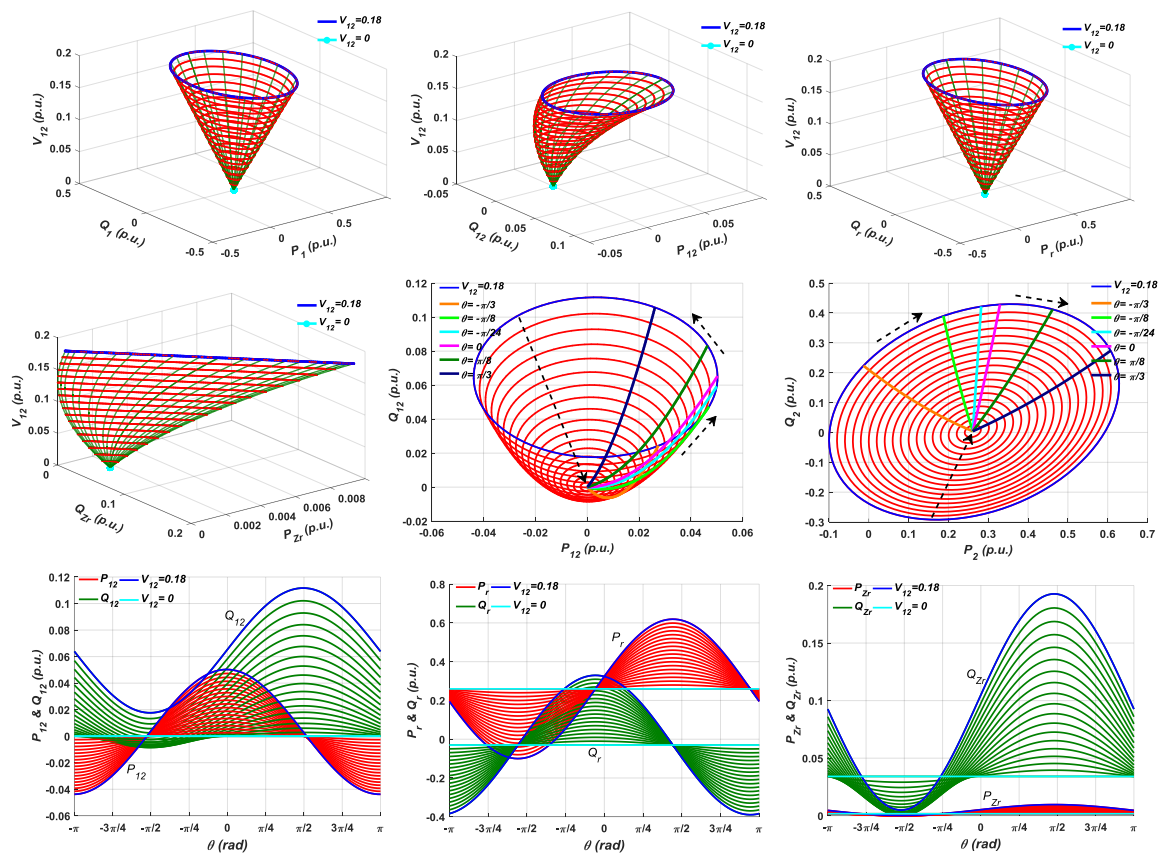
Figure 6. The power flow spatial operation surfaces and planes when $V_r = 1$, $\delta = -\pi/24$.

3.2.3. Power Flow Analyses Under Varying Condition 3 and Condition 4

In the following, we will continue to research the impact of the variation of the voltage magnitude on the UPFC regulation. Firstly, we assume there is a 10% descent of the voltage magnitude of the receiving end bus, but the phase δ still remains invariant, namely, $V_r = 0.9$, $\delta = -\pi/8$. The resulting figures are all shown in Figure 7.

In this case, it can be seen no matter the structures of the spatial operation surfaces or the planes of each part, they are more similar to those of the normal condition, although there may be a little decrease in the operation areas of each part. Upon the above situation, we have also investigated the condition when there is a 10% increase of V_r, namely $V_r = 1.1$, $\delta = -\pi/8$. We have also obtained the similar results as the above condition except for a little increase in the operation areas of each part.
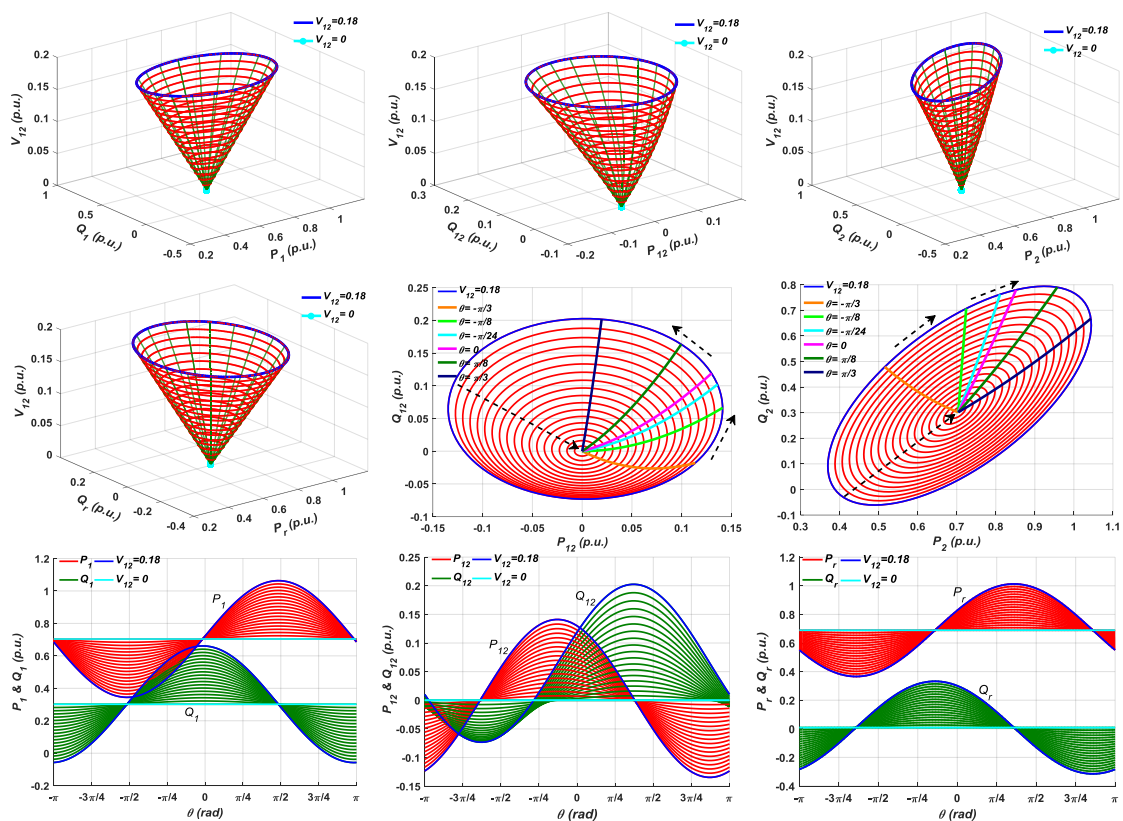
Figure 7. The power flow spatial operation surfaces and planes when $V_r = 0.9$, $\delta = -\pi/8$.

The results of the two conditions above indicate that the variation of the voltage magnitude of the receiving end bus V_r has not obvious influence on the power flow regulation by UPFC.

3.2.4. Power Flow Analyses under the Worst Condition 5

Finally, we will consider the worst condition that the voltage magnitude of the receiving end bus has a sharp decrease of 18% and the phase δ has a large increase, namely, $V_r = 0.82$, $\delta = -\pi/2$. The results are all listed in Figure 8 as well.

Above all, we can see that the areas of the spatial surfaces of each part have all reached the maximum of all the researched conditions. Then the power flow ranges of v_{12} have reached about 0.5 p.u., and the lower half region of v_{12} has increased significantly which has nearly become symmetric with the upper half region. Moreover, the real power on the receiving end impendence P_{Zr} has reduced to very small value compared to that of the reactive power Q_{Zr}. The results indicate that although the transfer capacity of the real power flow of the system has almost reached the maximum among the discussed conditions, the UPFC can provide enough strong support of the reactive power for the receiving end bus, to maintain the regular power flow of the system under the worst condition.

For another aspect, the elliptical closed-loops of series side bus$_2$ P_2—Q_2 in the operation plane have inversely moved in the counterclockwise direction as the same as v_{12}, and the varying rate of P_2 has also increased apparently, there also emerges some regions of intersections in the plane. The results may be an implication that the system has arrived at the neighbor of the critical stable point, and the regulation capability of UPFC has also reached its maximum—0.5 p.u., which is about double or more of the normal condition; however, in general, this capacity is still feasible and practicable in application, and the capability of UPFC is still enough to ensure the stable operations of the systems.
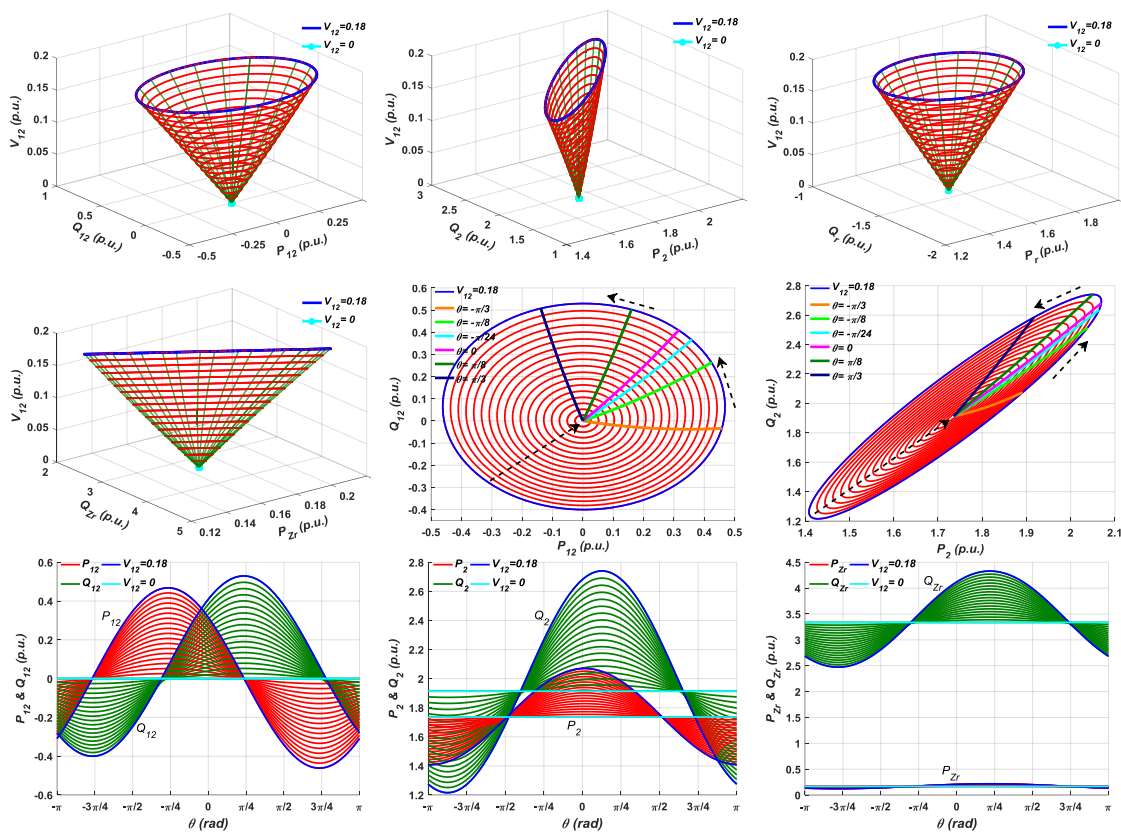
Figure 8. The power flow spatial operation surfaces and planes when $V_r = 0.82$, $\delta = -\pi/2$.

3.3. Obtained Power Flow Principles

So far, we have completed all the power flow analyses of the system under several typical conditions, and the following power flow principles may be summarized.

1. The power flow operation traces of UPFC of each part along the line in the plane are closed and restricted mutually. The power flow capacities of each part are proportional to the magnitude of v_{12}. More regions of intersections of the real and reactive power in the plane may indicate more intense fluctuations and higher THD of power qualities of the system. The shape and area of the spatial operation surfaces also reflect the regulation capacity and capability of UPFC presently.

2. The regulation of UPFC is mainly achieved through the series embedded voltage v_{12}, but the power flow moving traces of v_{12} along the elliptical traces are contrary to the other parts, implying the control method of v_{12} is different and special.

3. When the phase δ of the receiving end decrease to certain degrees, there may appear much more regions of intersections in the operation planes and more seriously bended and inclined spatial operation surfaces of v_{12}, indicating the regulating capabilities of UPFC may descend obviously, and the reactive power support for the receiving end may become weaker under this condition.

4. The variations of the voltage magnitude of the receiving end bus V_r have no obvious influence on the power flow regulation by UPFC, but only change the power flow capacity of each part along the line.

5. Under the worst condition when $V_r = 0.82$, $\delta = -\pi/2$, the test system has arrived at the neighbor of the critical stable point where the transfer capacity of the real power flow of the system has almost reached the maximum, but the UPFC can provide enough strong support of the reactive power for the receiving end bus, and the maximal capacity of UPFC is still feasible and practicable in application, thus ensuring the stable operation of the system.

Until now, we have obtained some important summarizations in the operating characteristics of UPFC under various conditions, by which the power flow dispatchers are able to get qualitative regulation references and estimations for regulating UPFC. Also, crucial indications for the subsequent control design of MMC-based UPFC had also been concluded, revealing that the control method should be adaptive to the special characteristics of v_{12} and the wide operation ranges under various conditions. The effectiveness and efficiency of the designed control scheme will be validated by the relevant simulation in the last section, which can also verify the agreement with the proposed power flow principles.

4. Control Design of MMC-Based UPFC Converters

As has been analyzed, the control method of UPFC is different and special to regulate the system under various conditions. Therefore, it is necessary to design a suitable control strategy for MMC-based UPFC to achieve satisfactory accuracy, response speed, and stability under various conditions.

First, in this section, we will design out the current and voltage control loops of both shunt and series converter in the complex domain, respectively, which will be used as the fundamental inner control loops, and then carry out the outer feedforward control parts to implement the whole control strategy, respectively.

4.1. Control Inner-loop Design of the Shunt Converter MMC 1

First, according to the detailed structural diagram of the shunt converter in Figure 9a and Kirchhoff laws, the voltage balance equation of shunt converter in a-b-c stationary frame are listed as below,

$$V_{1k} = V_{shk} + R_{sh}i_{shk} + L_{sh}di_{shk}/dt \ (k = a, b, c) \tag{11}$$
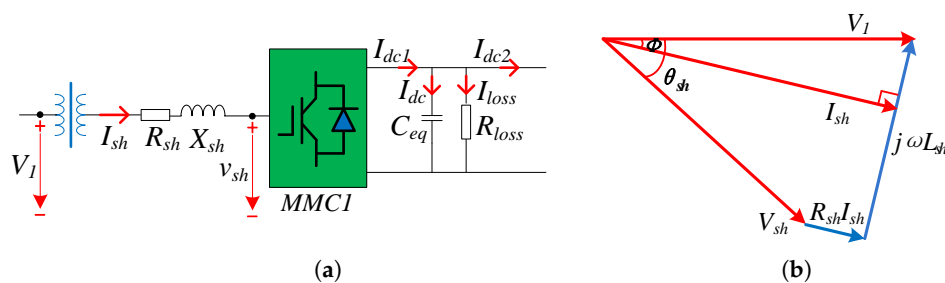
Figure 9. The detailed diagram of the shunt converter side. (**a**) The structural diagram; (**b**) The phasor diagram of the parameters.

By Park 3/2 transformation, the above equation in d-q rotating axes can be derived as follows,

$$\begin{cases} V_{1d} = V_{shd} + R_{sh}i_{shd} + L_{sh}di_{1d}/dt - \omega L_{sh}i_{shq} \\ V_{1q} = V_{shq} + R_{sh}i_{shq} + L_{sh}di_{1q}/dt + \omega L_{sh}i_{shd} \end{cases} \tag{12}$$

Based on the d-q balance equations, we can figure out the basic control scheme of the shunt converter as Figure 10 shows. The current inner-loops are based on the above d-q balance equations, and the two outer feedforward control blocks must provide the references for the d-axis and q-axis components of i_{sh}, respectively.
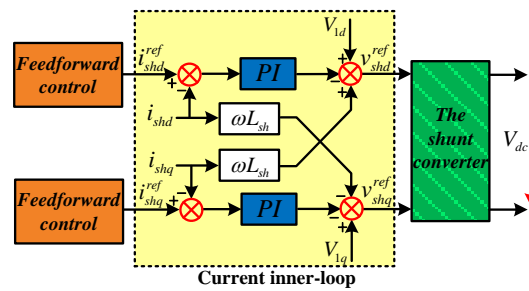
Figure 10. The basic control scheme of the shunt converter.

It should be noted that on account of the proportion effect of the PI controller, we can omit the turning ratio of the shunt transformer, and adopt the input voltage of the shunt converter just as V_1 in the voltage balance equation and control scheme.

Based on the scheme, firstly, we will carry out the initial current control inner-loop of shunt converter in the complex domain as Figure 11a displays. Here, K_{IP} and K_{II} stand for the proportion and integral parameters of PI controller, respectively, K_{NLM} and T_s represent the gain factor and time constant of MMC, respectively, L_{sh} and R_{sh} stand for the inductance and resistance at the grid side of the shunt MMC 1, and T_{If} means the sampling and feedback time delay. As the time constant T_{If} is usually a tiny value, the initial control loop can be transformed to one unity-feedback control loop, as shown in Figure 11b.

(a)   **(b)**
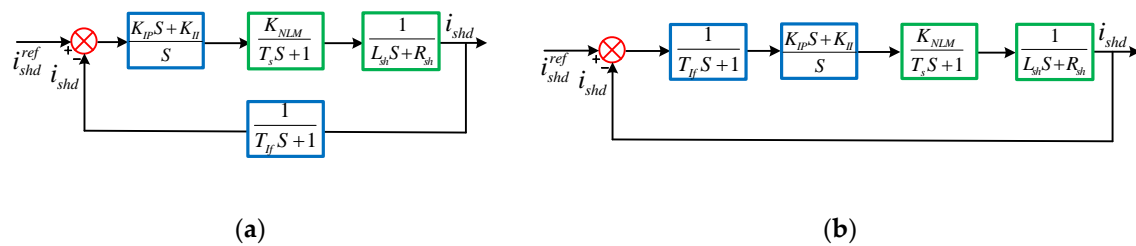
Figure 11. The current control loop of the shunt converter. (**a**) The initial current control loop; (**b**) The simplified unity-feedback current control loop.

On this basis, we can easily carry out the open-loop transfer function of the current inner-loop of shunt converter as below.

$$G_I(s) = \frac{K_{NLM}(K_{IP}s + K_{II})}{s(T_s s + 1)(T_f s + 1)(L_{sh}s + R_{sh})} \tag{13}$$

As is known, two smaller inertial elements can be merged into one bigger inertial model, so in the above transfer function (13), the two tiny time constant T_s and T_f can be merged into one time constant as $T_{Im} = T_s + T_{If}$. For further simplicity, we have also assumed that $K_{II}/K_{IP} = R_{sh}/L_{sh}$, and $K_{shI} = K_{IP}K_{NLM}/L_{sh}$, then the following expression can be derived,

$$G_{Ish}(s) = \frac{K_{shI}}{s(T_{Im}s + 1)} \tag{14}$$

As the structure of the open-loop function shows, the corresponding closed-loop transfer function should appear as a typical second-order resonant model as below,

$$C_{Ish}(s) = \frac{G_{Ish}(s)}{1 + G_{Ish}(s)} = \frac{K_{shI}}{T_{Im}s^2 + s + K_{shI}} = \frac{\omega_n^2}{S^2 + 2\xi\omega_n s + \omega_n^2} \tag{15}$$

Through observing and comparing, the following parameters can be deduced out, $K_{shI} = 1/(T_{Im}(2\xi)^2)$, $\omega_n = \sqrt{K_{shI}/T_{Im}}$, $K_{IP} = K_{shI}L_1/K_{NLM}$, $K_{II} = K_{IP}R_1/L_1$.

The primary parameters and performance of the current inner-loop in the complex and time domain have been listed in Tables 2 and 3, respectively.

Table 2. The design parameters and performance of the control loops in complex domain.

Components		Base Frequency (rad/s)	Damping Ratio	Magnitude Margin (dB)	Phase Margin (degree)	Resonance Peak (p.u.)	Bandwidth (dB)	Proportion of PI	Integral of PI	K_{NLM}
Shunt Converter	Current Inner-loop	1767.78	0.7071	Infinite	65.5299	1.0000	1787.53	1.9532	234.3795	1.6
	Feedforward loop-i_{shd}	314.159	0.4852	Infinite	50.6229	1.1785	408.89	1.6817	78.4770	1.6
	Feedforward loop-i_{shq}	200	0.7622	Infinite	68.2184	—	185.04	2.6240	131.1980	—
Series Converter	Current Inner-loop	1768.78	0.7071	Infinite	65.5299	1.0000	1787.53	2.4039	96.1557	1.3
	Voltage Outer-loop	314.159	0.5235	Infinite	53.6859	1.1209	394.09	0.7501	0	1.3
	Feedforward loop-v_{12q}	130	0.7212	Infinite	66.2534	—	127.9697	1.8025	90.1258	—
	Feedforward loop-v_{12d}	130	0.7212	Infinite	66.2534	—	127.9697	1.8025	90.1258	—

Table 3. The design parameters and performance of the control loops in time domain.

Components		Unit-Step Response				Velocity Error Constant
		Rising-Time	Max-Overshoot	Settling-Time	Resonant Cycles	
Shunt Converter	Current Inner-loop	0.0020	0.0427	0.0032	0.6366	1250.02
	Feedforward loop- i_{shd}	0.0076	0.1749	0.0260	0.7180	323.718
	Feedforward loop- i_{shq}	0.0190	0.0247	0.0280	0.5769	131.198
Series Converter	Current Inner-loop	0.0020	0.0427	0.0032	0.6366	1250.02
	Voltage Outer-loop	0.0080	0.1451	0.0244	1.0394	300.033
	Feedforward loop- v_{12q}	0.0266	0.0380	0.0454	0.6507	90.1258
	Feedforward loop-v_{12d}	0.0266	0.0380	0.0454	0.6507	90.1258

4.2. Feedforward Control Design of the Shunt Converter MMC 1

Based on the above current inner-loop, here we will continue to figure out the two feedforward control blocks related to the d-axis and q-axis components of i_{sh}, respectively, to further improve the stability and precision of the control loops.

4.2.1. Feedforward Control Block Related to the D-axis Component of I_{sh}

As is known, the back-to-back dc voltage V_{dc} of the MMC must maintain constant during the operation of UPFC, so it is mandatory to include V_{dc} in the feedforward input.

According to the operation principle of UPFC, the real power absorbed or applied by the series converter P_{se} must be compensated by the real power applied or absorbed by the shunt converter P_{sh}. Additionally, it had to take the real power losses P_{loss} conducted during the transition process into account so that the dc link voltage V_{dc} can be maintained constant more precisely. Thus, the real power balance equation can be listed as follows,

$$P_{sh} - P_{loss} = P_{se} \tag{16}$$

Accordingly, the equation can be further transformed as,

$$I_{shd} = V_{dc} I_{dc2} / V_1 + P_{loss} / V_1 \tag{17}$$

As the real power losses P_{loss} reflect the fluctuation of V_{dc} to some extent, here we can derive the reference of I_{shd} through a PI controller, whose expression can be designed as below,

$$I_{shd}^{ref} = (V_{dc}^{ref} - V_{dc})(k_{VP} + k_{VI}/s) + I_{dc2} \cdot V_{dc}/V_1 \tag{18}$$

By this expression of feedforward control design, we have related one voltage feedforward control block to the d-axis components of i_{sh}, as shown in Figure 12.
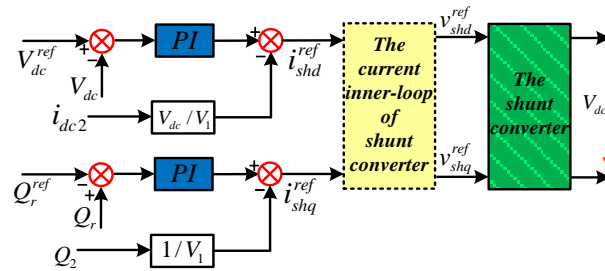
Figure 12. Diagram of the whole feedforward control scheme of the shunt converter.

To obtain the transfer function of the voltage control loop containing the voltage feedforward control block and evaluate its performance, we continue to make further derivation in the following part.

According to the phasor diagram in Figure 9b, we can assume the following equations,

$$\begin{cases} V_{1a} = V_1 \sin \omega t \\ V_{1b} = V_1 \sin(\omega t - 2pi/3) \\ V_{1c} = V_1 \sin(\omega t + 2pi/3) \end{cases} \begin{cases} I_{sha} = I_{sh} \sin(\omega t - \phi) \\ I_{shb} = I_{sh} \sin(\omega t - \phi - 2pi/3) \\ I_{shc} = I_{sh} \sin(\omega t - \phi + 2pi/3) \end{cases} \tag{19}$$

With the assumed expressions above, firstly, we can deduce the instantaneous power losses through the resistance R_{sh} at the shunt converter side as follows,

$$P_{shR} = \sum_{k=a,b,c} i_{shk}^2 \cdot R_{sh} = \left(i_{sha}^2 + i_{shb}^2 + i_{shc}^2\right) \cdot R_{sh} = \frac{3R_{sh}I_{sh}^2}{2} \tag{20}$$

Similarly, we can derive the instantaneous power of single-phase inductor as below,

$$P_{Lk} = L_{sh} i_{shk} \frac{di_{shk}}{dt} = \frac{L_{sh}}{2} \frac{di_{shk}^2}{dt} \ (k = a, b, c) \tag{21}$$

Accordingly, the power of all the three-phase inductors should be calculated as,

$$P_{shL} = \sum_{k=a,b,c} P_{Lk} = \sum_{k=a,b,c} L_{sh} i_{shk} \frac{di_{shk}}{dt} = \sum_{k=a,b,c} \frac{L_{sh}}{2} \frac{di_{shk}^2}{dt} = \frac{L_{sh}}{2} \frac{d(i_{sha}^2 + i_{shb}^2 + i_{shc}^2)}{dt} = \frac{3L_{sh}dI_{sh}^2}{4dt} \tag{22}$$

As is known, the instantaneous power injected into the dc side from the shunt converter can be presented as,

$$P_{dc1} = V_{dc} \cdot i_{dc1} \tag{23}$$

Also, the instantaneous power supplied by the shunt converter can be calculated as follows,

$$P_{sh} = \sum_{k=a,b,c} V_1 i_{shk} = V_1(i_{sha} + i_{shb} + i_{shc}) = \frac{3V_1 I_{sh} \cos \phi}{2} = \frac{3V_1 i_{shd}}{2} \tag{24}$$

Based on the energy balancing principles, the real power balancing equation transferring through the shunt converter can be listed as below,

$$P_{sh} = P_{shR} + P_{shL} + P_{dc1} \tag{25}$$

By combining Equations (20)–(25), we can obtain the following formula,

$$2V_{dc}i_{dc1}/3 = V_1 i_{shd} - R_{sh}I_{sh}^2 - L_{sh}I_{sh}dI_{sh}/dt \tag{26}$$

We can also list the current balancing equation based on the Kirchhoff current law as below,

$$i_{dc1} = C_{eq}du_{dc}/dt + u_{dc}/R_{loss} \tag{27}$$

Here, we may assume certain small signal fluctuations on the initial value of specified parameters as, $i_{dc1} = I_{dc1}^0 + \Delta i_{dc1}$, $I_{sh} = I_{sh}^0 + \Delta I_{sh}$, $V_{dc} = V_{dc}^0 + \Delta V_{dc}$.

Where, the superscript 0 stands for the constant part of the parameters, and the Δ symbols represent the small vibrations. Then we carried out the following equations,

$$\begin{cases} \Delta i_{dc1} = 3(V_1\Delta i_{shd} - 2R_{sh}I_{sh}^0\Delta I_{sh} - L_{sh}I_{sh}^0 d\Delta I_{sh}/dt)/2V_{dc}^0 \\ \Delta i_{dc1} = C_{eq}d\Delta u_{dc}/dt + \Delta u_{dc}/R_{loss} \end{cases} \tag{28}$$

Here, due to the voltage V_1 was mainly determined by the component of i_{shq}, we should assume i_{shq} to be constant so as to maintain V_1 stably, namely, $\Delta I_{sh} = \Delta i_{shd}$, then the transfer function of V_{dc} with respect to i_{shd} can be derived as follows,

$$\frac{\Delta V_{dc}(s)}{\Delta i_{shd}(s)} = K_T \frac{-T_{dc}s + 1}{T_{shd}s + 1} \tag{29}$$

Here, we have $T_{dc} = L_{sh}I_{sh}^0/(V_1 - 2R_{sh}I_{sh}^0) = L_{sh}/(R_{shin} - 2R_{sh})$, $K_T = 3R_{loss}(V_1 - 2R_{sh}I_{sh}^0)/4V_{dc}^0$, $T_{shd} = R_{loss}C_{eq}/2$.

Under normal conditions, it usually has the relation $V_1 \gg 2R_{sh}I_{sh}^0$, so the coefficient K_T can be simplified to $K_T = 3R_{loss}V_1/4V_{dc}^0$, and $R_{shin} = V_1/I_{sh}^0$ represents the input resistance of shunt converter.

It can be seen that the zero, pole and open-loop gain of this transfer function are all constant, and the zero point is only related to the input resistance of shunt converter, thus providing advantages to design the voltage outer-loops containing the current inner-loop, as shown in Figure 13a.

(a)

(b)
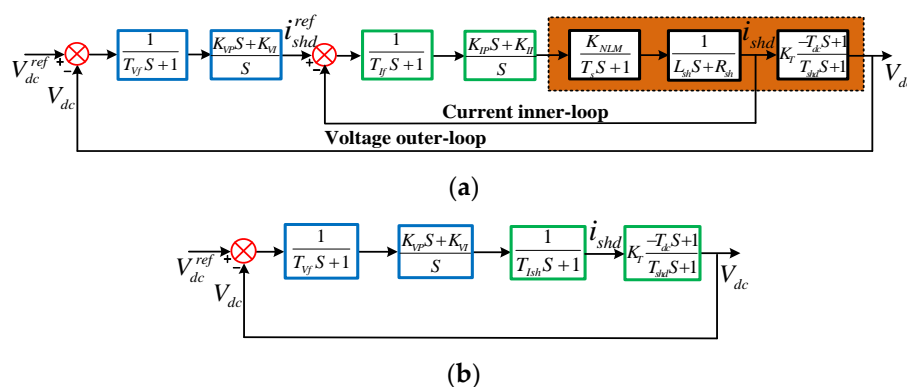
Figure 13. The double voltage control loops of shunt converter. (**a**) The initial double control loops; (**b**) The simplified unity-feedback voltage control loop.

For simplicity and convenience, we can just simplify the internal current control block to one first-order inertial process. Consider the bandwidth and basic frequency of the current inner loop will

be designed much larger than that of the voltage outer-loop, this simplification may not exert much impact and errors on the voltage outer-loop. The simplified transfer function of the inner-loop can be expressed as,

$$C_{sh}(s) = 1/(T_{Ish}s + 1) \tag{30}$$

Here, the time constant is assumed as $T_{Ish} = L_1/K_{Ip}$. Thus, the double voltage control loops above can be simplified to one unity-feedback voltage control loop, as shown in Figure 13b.

Accordingly, the open-loop transfer function of the voltage control loop is shown as follows,

$$G_{Vsh}(s) = \frac{K_0(K_{VP}s + K_{VI})(1 - T_{dc}s)}{s(T_{Ish}s + 1)(T_{shd}s + 1)(T_{vf}s + 1)} \tag{31}$$

Here, for further simplification, we assumed $K_{Vp}/K_{VI} = T_p$, $K_{shV} = K_T K_{VI}$ and $T_p = T_{shd}$, then we also merged the time constant T_{Ish} and T_{Vf} into one constant as similar to before, namely, $T_{Vm} = T_{Ish} + T_{Vf}$. Moreover, we also have the relation of $T_{dc} << T_{shd}$ in general. On the basis, we can derive the simplified transfer function as below,

$$G_{Vsh}(s) = \frac{K_{shV}}{s(T_{Vm}s + 1)} \tag{32}$$

Similarly, the corresponding closed-loop transfer function can be deduced, which also presents as one typical second-order resonant model,

$$C_{Vsh}(s) = \frac{G_{Vsh}(s)}{1 + G_{Vsh}(s)} = \frac{K_{shV}}{T_{Vm}s^2 + s + K_{shV}} = \frac{\omega_n^2}{S^2 + 2\xi\omega_n s + \omega_n^2} \tag{33}$$

Here, we can also derive out the parameters of K_{shV} and ω_n through observation and comparison, just the same as equation (15). The performance of the voltage control loop containing the feedforward control blocks related to i_{shd} had also been listed in Tables 2 and 3 later.

4.2.2. Feedforward Control Block Related to the Q-axis Component of I_{sh}

Next, we will continue to implement another feedforward control block related to the q-axis component of i_{sh}.

According to the UPFC structural diagram in Figure 1a, the reactive power balance equation can be listed as follows,

$$Q_{1s} + Q_{12} - Q_{sh} = (Q_1 + Q_{sh}) + Q_{12} - Q_{sh} = Q_1 + Q_{12} = Q_2 \tag{34}$$

Here, $Q_{1s} = imag(\dot{V}_1 \cdot \dot{I}_s^*)$ and $Q_{sh} = imag(\dot{V}_1 \cdot \dot{I}_{sh}^*)$ stand for the reactive power transferring from the sending end source and the reactive power absorbed by the shunt converter, respectively.

As V_1 is assumed to maintain constant, here we can extend the above balance equation in the d-q rotating axes as,

$$imag[V_1(i_{sd} + ji_{sq})^* + (v_{12d} + jv_{12q})(i_{1d} + ji_{1q})^* - V_1(i_{shd} + ji_{shq})^*] = Q_2 \tag{35}$$

After deducing, it is easy to obtain the following equation,

$$V_1 i_{shq} = V_1 i_{sq} + v_{12q} i_{1d} - v_{12d} i_{1q} - Q_2 \tag{36}$$

Here, we also assumed certain small signal fluctuations on the initial value, such as $i_{sq} = i_{sq}^0 + \Delta i_{sq}$, $i_{1d} = i_{1d}^0 + \Delta i_{1d}$, $i_{1q} = i_{1q}^0 + \Delta i_{1q}$, $v_{12d} = v_{12d}^0 + \Delta v_{12d}$, $v_{12q} = v_{12q}^0 + \Delta v_{12q}$, and $Q_2 = Q_2^0 + \Delta Q_2$.

Then through calculation, we can acquire the small signal model of the reactive power balance equation,

$$\Delta i_{shq} = \Delta i_{sq} + (v_{12q}^0 \Delta i_{1d} - v_{12d}^0 \Delta i_{1q} + v_{12q} \Delta i_{1d}^0 - v_{12d} \Delta i_{1q}^0)/V_1 - \Delta Q_2/V_1 \tag{37}$$

It can be seen that the first two parts of the right side of the equation (37) stand for the reactive current variations supplied by the power source and the series converter, respectively, and the last part represents the reactive current variations through the receiving end bus.

Therefore, to maintain V_1 constant, the reactive current variation of the shunt converter must compensate the reactive power absorbed by the series converter and the receiving end line. However, Q_{12} cannot be determined by Q_{sh}, then the variations of the reactive current of the series converters should be compensated by Q_2. Furthermore, as we have the relation $Q_2 + Q_{Zr} = Q_r$, and the reactive power losses of the receiving end impendence Q_{zr} can be compensated by one PI controller, we can just take the reactive power of the receiving end Q_r as the feedforward control input, which is related to the q-axis component of i_{sh} through a PI controller.

$$i_{shq}^{ref} = -(Q_r^{ref} - Q_r)(k_{IP} + k_{II}s) - Q_2/V_1 \tag{38}$$

As with the simplified unity-feedback voltage loop, we can directly design the simplified unity-feedback reactive power loop, as shown in Figure 14.
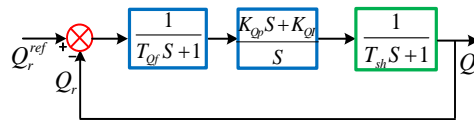
Figure 14. The unity-feedback reactive power control loop of the shunt converter.

Here, it is assumed $K_{QP}/K_{QI} = T_{Qf}$, to eliminate a pair of zero-pole points, thus the open-loop transfer function can be expressed as,

$$G_{Qsh}(s) = \frac{K_{QP}s + K_{QI}}{s(T_{Qf}s + 1)(T_{sh}s + 1)} \approx \frac{K_{QI}}{s(T_{sh}s + 1)} \tag{39}$$

Consequently, the closed-loop transfer function is as follows,

$$C_{Qsh}(s) = \frac{G_{Qsh}(s)}{1 + G_{Qsh}(s)} = \frac{K_{QI}/T_{sh}}{s^2 + (1/T_{sh})s + K_{QI}/T_{sh}} \tag{40}$$

The performance of the reactive power control loop containing the feedforward control blocks related to i_{shq} had also been listed in Tables 2 and 3.

Based on the feedforward controllers, we can figure out the whole control scheme of the shunt converter, as depicted in Figure 12.

4.3. Double Inner-loop Design of the Series Converter MMC 2

As the similar method as the shunt converter, firstly we also listed the detailed structural diagram of series converter, as is shown in Figure 15.
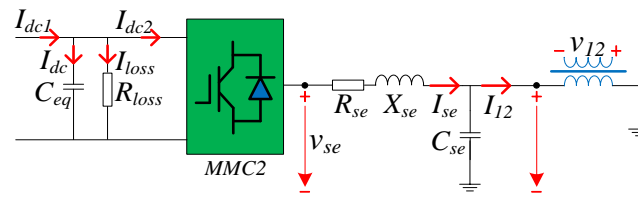
Figure 15. The detailed structural diagram of the series converter.

According to the diagram above, we can list the voltage and current balance equations in a-b-c stationary frame as below, respectively. Please note that the turn ratio of the series transformer can also be compensated by a PI controller, thus we can still use v_{12} in the voltage balance equations.

$$\begin{cases} V_{sek} = V_{12k} + R_{se}i_{sek} + L_{se}di_{sek}/dt \ (k = a, b, c) \\ i_{sek} = i_{12k} + C_{se}dv_{12k}/dt \ (k = a, b, c) \end{cases} \tag{41}$$

Through Park 3/2 transformation, we can also derive the balance equations in d-q rotating axes as below.

$$\begin{cases} V_{sed} = V_{12d} + R_{se}i_{sed} + L_{se}di_{sed}/dt - \omega L_{se}i_{seq} \\ V_{seq} = V_{12q} + R_{se}i_{seq} + L_{se}di_{seq}/dt + \omega L_{se}i_{sed} \end{cases} \begin{cases} i_{sed} = i_{12d} + C_{se}dv_{12d}/dt - \omega C_{se}v_{12q} \\ i_{seq} = i_{12q} + C_{se}dv_{12q}/dt + \omega C_{se}v_{12d} \end{cases} \tag{42}$$

Accordingly, we can carry out the basic control scheme based on the equations above, as depicted in Figure 16a. The structure of the current inner-loop is almost the same as the shunt converter, except for one additional voltage outer-loop on account of the earth capacitor C_{se}.

Similarly, we can figure out the double voltage loop of the series converter, as is shown in Figure 16b.

As the same as before, the current inner-loop can also be simplified to one first-order inertial process, whose transfer function can be expressed as below,

$$C_{se}(s) = 1/(T_{Ise}s + 1) \tag{43}$$

Here, it is assumed that the equivalent time constant can be evaluated by $T_{Ise} = L_2/K_{Ip}$, then we can carry out the unity-feedback loop of the series converter as Figure 16c depicts.

Similarly, after merging the two smaller time constants into $T_{Vm} = T_{Vf} + T_{Ish}$, the open-loop transfer function can be expressed as below,

$$G_{Vse}(s) = \frac{K_{VP}s + K_{VI}}{C_{se}s^2(T_{Vm}s + 1)} \tag{44}$$

As can be seen, consider the characteristic equation of the closed-loop function will reach three order, we attempted to degrade it to the typical second-order system after setting K_{VI} as zero, then the degraded closed-loop transfer function was derived as below,

$$C_{Vse}(s) = \frac{G_{Vse}(s)}{1 + G_{Vse}(s)} = \frac{K_{VP}s + K_{VI}}{C_{se}T_{Vm}s^3 + C_{se}s^2 + K_{VP}s + K_{VI}} = \frac{1}{(C_{se}T_{Vm}/K_{VP})s^2 + (C_{se}/K_{VP})s + 1} \tag{45}$$

Here, the basic frequency of the system and the parameters of PI controller are derived as $\omega_n = \sqrt{K_{VP}/C_{se}T_{Vm}}$, $K_{VP} = C_{se}/(T_{Vm}(2\xi)^2)$, $K_{VI} = 0$.
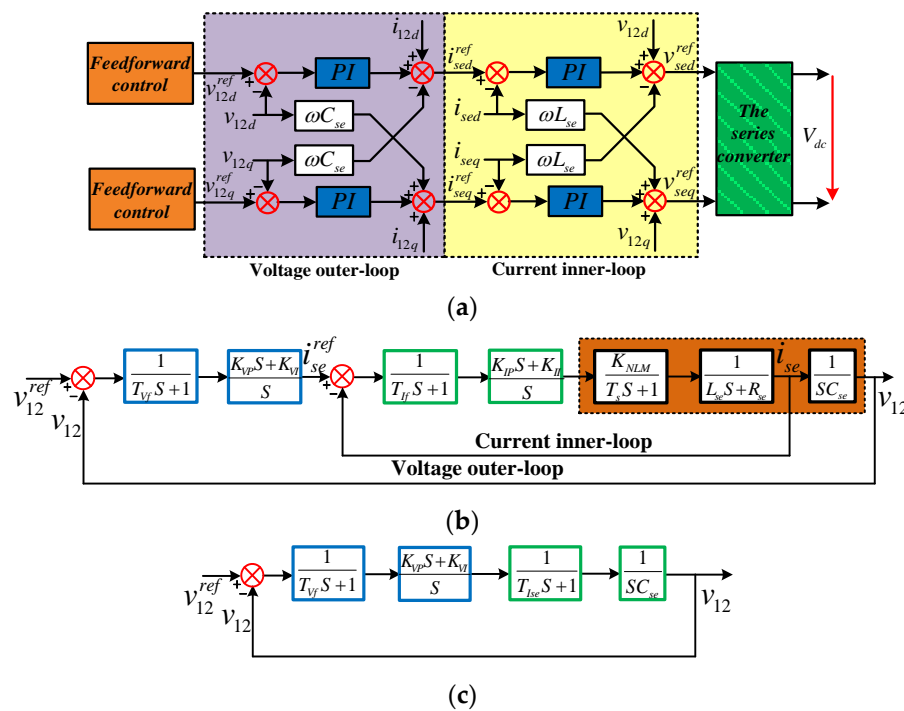
Figure 16. Diagrams of the basic control scheme and loops of the series converter. (**a**) The basic control scheme; (**b**) The initial double control loops; (**c**) The simplified unity-feedback control loop.

4.4. Feedforward Control Design of the Series Converter MMC 2

4.4.1. Feedforward Control Block Related to the D-axis Component of V_{12}

Based on the basic control scheme, we also must implement two feedforward control blocks related to the d-axis and q-axis components of v_{12}.

Firstly, we will list the reactive power of the series side bus 2 once again in d-q rotating axes, which can be derived by the following equation,

$$
\begin{aligned}
Q_2 &= imag(\dot{V}_2 \cdot \dot{I}_1^*) = imag\{(\dot{V}_1 + \dot{V}_{12})[(\dot{V}_1 + \dot{V}_{12} - \dot{V}_r)/jX_r]^*\} \\
&= -[V_1^2 + V_{12}^2 + v_{12q}v_{rq} - V_1 v_{rd} + (2V_1 - v_{rd})v_{12d}]/X_r
\end{aligned}
\tag{46}
$$

Normally, the difference between V_1 and V_r in magnitude and phase is always small, thus it can be inferred that $2V_1 - v_{rd} >> v_{rq}$. Therefore, the best way to control Q_2 is by the v_{12d} which has the predominant influence on Q_2.

However, just as equation (34) shows, the reactive power Q_{12} is not controllable by Q_{sh}, but Q_2 is influenced by Q_{sh} while Q_{sh} has a determinate impact on maintaining V_1 constant. Thus, it is necessary to find another way to supply a reference to v_{12d} by V_1.

According to the phasor diagram, we can easily list the voltage balance equations as below,

$$
V_{1k} + V_{12k} = V_{rk} + R_r i_{1k} + L_r di_{1k}/dt \ (k = a, b, c)
\tag{47}
$$

Then the voltage equations in d-q rotating axes can also be yielded through the Park 3/2 transformation,

$$
\begin{cases}
V_1 = V_{rd} + R_r i_{1d} + L_r di_{1d}/dt - \omega L_r i_{1q} - V_{12d} \\
0 = V_{rq} + R_r i_{1q} + L_r di_{1q}/dt + \omega L_r i_{1d} - V_{12q}
\end{cases}
\tag{48}
$$

From the first part of equation (48), we can design a PI control block related to v_{12d} as the following formula shows,

$$
v_{12d}^{ref} = -(V_1^{ref} - V_1)(k_{VP} + k_{VI}/s) - \omega L_r i_{1q}
\tag{49}
$$

Similarly, we can figure out the corresponding control loop including the feedforward blocks as Figure 17a, and list the open-loop and closed-loop transfer functions as below.

$$G_{V_1se} = \frac{K_{VP}s + K_{VI}}{s(T_{Vf}s+1)(T_{se}s+1)} \approx \frac{K_{VI}}{s(T_{se}s+1)} \tag{50}$$

$$C_{V_1se} = \frac{G_{V_1se}}{1+G_{V_1se}} = \frac{K_{VI}/T_{se}}{s^2 + (1/T_{se})s + K_{VI}/T_{se}} \tag{51}$$

(**a**)   (**b**)
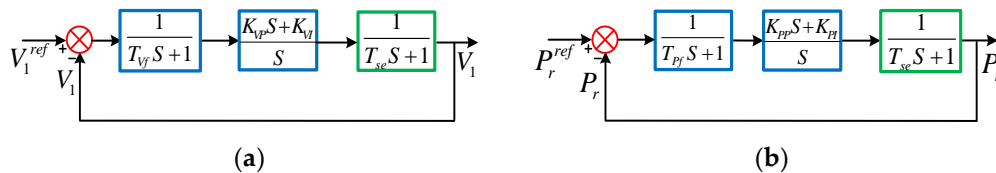
Figure 17. Diagrams of the unity-feedback control loops including the feedforward blocks of the series converter. (**a**) The voltage control loop including the feedforward blocks related to v_{12d}; (**b**) The active power control loops including the feedforward blocks related to v_{12q}.

4.4.2. Feedforward Control Block Related to the Q-axis Component of V_{12}

Next, we continue to design the other feedforward block related to v_{12q}. As the real power of series side bus 2 can be expressed as,

$$\begin{aligned} P_2 = real(\dot{V}_2 \cdot \dot{I}_1^*) &= real\{(\dot{V}_1 + \dot{V}_{12})[(\dot{V}_1 + \dot{V}_{12} - \dot{V}_r)/jX_r]^*\} \\ &= real\{(\dot{V}_1 + \dot{V}_{12})\dot{V}_r^*/jX_r\} = [(V_1 + v_{12d})v_{rq} + v_{12q}v_{rd}]/X_r \end{aligned} \tag{52}$$

After the Park 3/2 transformation, the most right-side expression of equation (52) can be obtained. As usual, it generally has the relation $v_{rd} >> v_{rq}$, so that the varying of v_{12q} has much larger impact on P_2 than that of v_{12d}, so it is more reasonable and accurate to provide the reference for v_{12q} by P_2. Moreover, as the real power losses of receiving end impendence P_{zr} can also be compensated by the PI controller, we can just use P_r instead of P_2 based on the relation $P_2 + P_{zr} = P_r$. Therefore, we can figure out the feedforward control blocks related to v_{12q} by P_r based on one PI controller.

$$v_{12q}^{ref} = (P_r^{ref} - P_r)(k_{PP} + k_{PI}/s) \tag{53}$$

Similarly, we can also carry out the corresponding control loop including the feedforward blocks related to v_{12q} as Figure 17b show, of which the open-loop and closed-loop transfer functions are also listed as follows.

$$G_{Pse} = \frac{K_{PP}s + K_{PI}}{s(T_{Pf}s+1)(T_{se}s+1)} \approx \frac{K_{PI}}{s(T_{se}s+1)} \tag{54}$$

$$C_{Pse} = \frac{G_{Pse}}{1+G_{Pse}} = \frac{K_{PI}/T_{se}}{s^2 + (1/T_{se})s + K_{PI}/T_{se}} \tag{55}$$

Here, we also assume that $K_{VP}/K_{VI} = T_{Vf}$, and $K_{PP}/K_{PI} = T_{Pf}$. The meanings of the other parameters are as similar to before.

Based on the above design, we can work out the whole feedforward control scheme of the series converter, as shown in Figure 18.
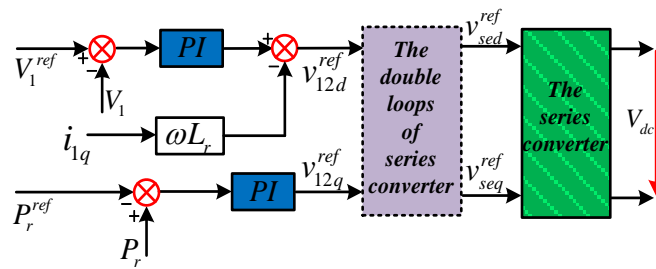
Figure 18. The whole feedforward control scheme of the series converter.

Until now, we have achieved all feedforward control blocks and schemes for both the shunt and series converters. On the basis, the feedforward control blocks will provide requisite references with the introduction of necessary compensating branches for the input components of the inner-loops, thus coordinating the d-axis and q-axis components of the inner-loops related to the variation of the real and reactive power, respectively.

4.5. Analyses of the Control Strategy in Complex and Time Domain

To analyze the characteristics and performance of the proposed control strategy, first, we must assume some basic settings. In general, to obtain favorable waveforms and satisfactory response speed, the damping ratio of current inner-loops are fixed at 0.7071, and the basic frequency of voltage outer-loops are set as 314.159, which are similar to the power frequency so that the controllers can interact with the ac grids smoothly. The converter time delay and the feedback filtering and sampling delay are all set as $T_s = T_{If} = T_{Vf} = 0.2$ *ms*, the available submodule number of MMC is provided as 28, and the equivalent capacitance of MMC is about 2.0e4 μF through deriving. The modulation ratios of the MMC are both set as Table 2 show. The back-to-back dc voltage is 20 kV, and the nominal voltage of the system is 220 kV.

All the resulting performance of the parameters of the designed control loops in the complex and time domain have been listed in Tables 2 and 3, respectively.

As can be seen, the bandwidths of the inner-loops of both the shunt and series converters have reached about 5 times of those of the outer-loops. While the operation ranges of the outer-loops mainly locate at the lower frequency region, but those of the inner-loops are much wider and higher, ensuring that the operation of the outer-loops and inner-loops will scarcely interfere with each other.

From the time domain, it can be seen that the settling times of the inner-loops are more than seven times shorter than those of the outer-loops containing the feedforward control blocks, meaning that the response speed of the inner-loops is the fastest in the unit-step response. In addition, the control inner-loops operate with the widest bandwidth in the highest frequency regions and response with the smallest max-overshoots and errors. In contrast, the outer-loops containing the feedforward control blocks present narrower bandwidth in the lower operating frequency regions, also with the slower response speed and larger error. The results ensure that the inner-loops and the outer-loops regarding the feedforward blocks will operate without interfering each other much, thus more stable and precise output will be carried out.

Furthermore, it can be seen that the phase margins of the control loops almost range from 50 degrees to 70 degrees, which are usually satisfactory performances in the complex domain. The damping ratios of all the components are within 0.48 to 0.76, and the resonance peaks are not beyond 0.2 p.u. of the nominal value, which are all within the reasonable scopes. Thus, all the results had verified the favorable characteristics of the control schemes. It should be pointed out that the performance of the current inner-loops of the series converter is identical to that of the shunt converter, only except for the parameters of PI controllers and modulation ratios. Also, the two control loops regarding the feedforward blocks of the series converter have the same characteristic performance.

We have also depicted some typical figures of the characteristic performance of all the control components, as shown in Table A1 of Appendix A. From the figures, we can observe the performance of all the control components intuitionally, which coincides with the theoretical analyses.

The inadequacies of the control design may lie in that the damping ratios of the control loops regarding the feedforward blocks are a little bigger, resulting in that the response speed of the feedforward blocks may be a little slower, and the error constants may be somewhat insufficient. Although these defects are inevitable, they have scarcely any influence on the other primary performance.

So far, we have achieved the control design and analyses of all the components for MMC-based UPFC, the effectiveness of which will be validated by the following simulation.

5. Simulation Verification and Analyses

5.1. Simulation Design of Primary Parameters and Cases

In this section, to demonstrate the efficiency of the proposed control strategy and the agreement with the proposed power flow principles, a 220 kV two-ends power system embedded MMC-based UPFC was built and simulated by PSCAD. The designated structure is depicted by Figure 19 and the primary parameters are listed as Table 4. It can be seen that the distance between the sending end source and shunt side bus 1 is set 1km and the transmission line from series side bus 2 to receiving end is assumed as 100 km. The shunt side MMC 1 was supported by the 35 kV substation which was chopped down from voltage bus 1. In addition, we can also see some notations of faults set at the specified positions along the transmission line.
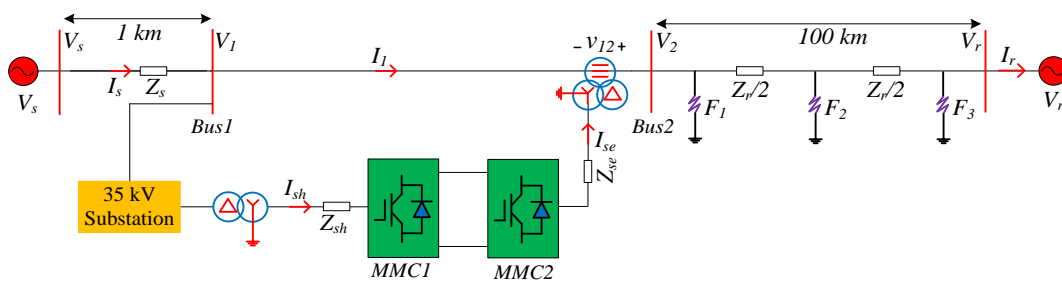
Figure 19. The structural diagram of the tested system in simulation.

Table 4. The primary parameters of MMC-based UPFC set in simulation.

Components	Parameters	Settings	Components	Parameters	Settings
The 35 kV substation of sending end	Rated capacity	120 MVA	The shunt transformer	Rated capacity	120 MVA
	Turn ratios	$220 \pm 2 \times 2.5\%/36.75$ kV		Turn ratios	$35 \pm 2 \times 2.5\%/20.2$ kV
	Leakage reactance	0.1 p.u.		Leakage reactance	0.1 p.u.
	Impendence from substation to shunt converter	$0.1 + j0.5 \, \Omega$		Group of joining	Δ/Yd11
MMC	No. of submodule	$30 - 2 = 28$ (2 redundancy)	The series transformer	Rated capacity	120 MVA
	Rated capacity	100 MVA		Turn ratios	166.5/20.8/10 kV
	Rated dc voltage	$\pm$ 20 kV		Leakage reactance	0.2/0.3/0.075 p.u.
	Average device switching frequency	about 1047 Hz		Group of joining	III/Yd11/Δ
	Capacitance of submodule	9.33e4 μF			

In the simulation, three cases considering different types of incidents will be carried out, respectively, the incidents of each case at the specified moments are all listed in Table 5. It should also be pointed out that circulating current suppressing controller (CCSC) in [34] was adopted in the MMC model for a better performance.

Table 5. The incidents of each case set in simulation.

	Moments	Incidents
Case1	0 s	$Pref = 0.6, Qref = -0.2$
	1.0 s	$Pref = 1.0, Qref = -0.2$
	1.5 s	$Pref = 1.0, Qref = -0.6$
	2.0 s	$Pref = 0.2, Qref = -0.6$
	2.5 s	$Pref = 0.2, Qref = -0.1$
	3.0 s	$Pref = -0.1, Qref = -0.1$
	3.5 s	$Pref = -0.1, Qref = 0.1$
	4.0 s	$Pref = 0.6, Qref = -0.2$
Case2	0 s	$Pref = 0.6, Qref = -0.2, v_r = 1, \delta = -\pi/8$
	1.0 s	$V_r = 1, \delta = -\pi/3$
	1.5 s	$V_r = 1, \delta = -\pi/24$
	2.5 s	$V_r = 1, \delta = \pi/24$
	3.5 s	$V_r = 0.9, \delta = -\pi/8$
	4.0 s	$V_r = 1.1, \delta = -\pi/8$
	4.5 s	$V_r = 0.82, \delta = -\pi/2$
Case3	0 s	$Pref = 0.6, Qref = -0.2, v_r = 1, \delta = -\pi/8$
	1.0 s	Single-phase ground fault of F1
	1.5 s	Three-phase ground fault of F1
	2.0 s	Single-phase ground fault of F2
	2.5 s	Three-phase ground fault of F2
	3.0 s	Single-phase ground fault of F3
	3.5 s	Three-phase ground fault of F3
	4.5 s	Sudden load increase and shedding of F3

5.2. Simulation Results and Analyses

5.2.1. Case 1: Steady-State Response upon Variation of Power Flow References

In case 1, it is provided that the power flow references of the receiving end were regulated by the dispatcher at the specified moments as shown in Table 5. The simulation results of case 1 were displayed in Figure 20, from which we can observe that when the power flow references of the receiving end were being regulated by the dispatcher, the real and reactive power fluctuations of each critical part were all able to decay to zero within 100ms, and the fluctuation ranges were almost within 0.1 p.u.. Among all the parts, the power flow of v_{12} had the most intense oscillation, which, however, could damp out within about 20ms-40ms. Moreover, the tracking errors of most parts could keep in a very small scale after the power flow recovered a steady state through estimation, validating the fast responses and high precisions of power flow regulation by MMC-based UPFC.

We can also view that the voltage and current of back-to-back dc lines only fluctuated a little in the neighbor of the 1 p.u. base line as the power flow varied, the varying ranges of dc voltage were always limited within 5% p.u.. The d-axis component and q-axis component of v_{12} both appeared to step up and down, but both of their magnitudes had not varied much in the process, and accordingly, the magnitude of v_{12} also presented a similar trend. However, the most significant fluctuating parameter was the phase θ of v_{12}, which varied most intensely at the moments of real power changing, implying that the regulation of the real power flow may be the main goal function and achievement, while the variation of reactive power reference might not impact the UPFC so apparently compared to the real power. Consequently, the current through the line I_1 and the magnitude of V_2 also fluctuated along with the regulating of UPFC, to adapt the power flow changes instantaneously. However, the magnitudes of V_1 and V_r always kept within very near neighbors of 1 p.u. during the whole simulation, verifying the efficiency and stability of voltage regulating by MMC-based UPFC.

The figures also show the THD of several parameters, it can be seen that the THD of most parameters maintained below 1% under steady-state, although the THD of the MMC output currents may be somewhat larger, they are also around 3%, validating the excellent converting performance of

MMC. It should also be pointed out that the measured THD during the transient periods of the incidents may not represent the actual performance, but just provide an intuitional and continuous graph.
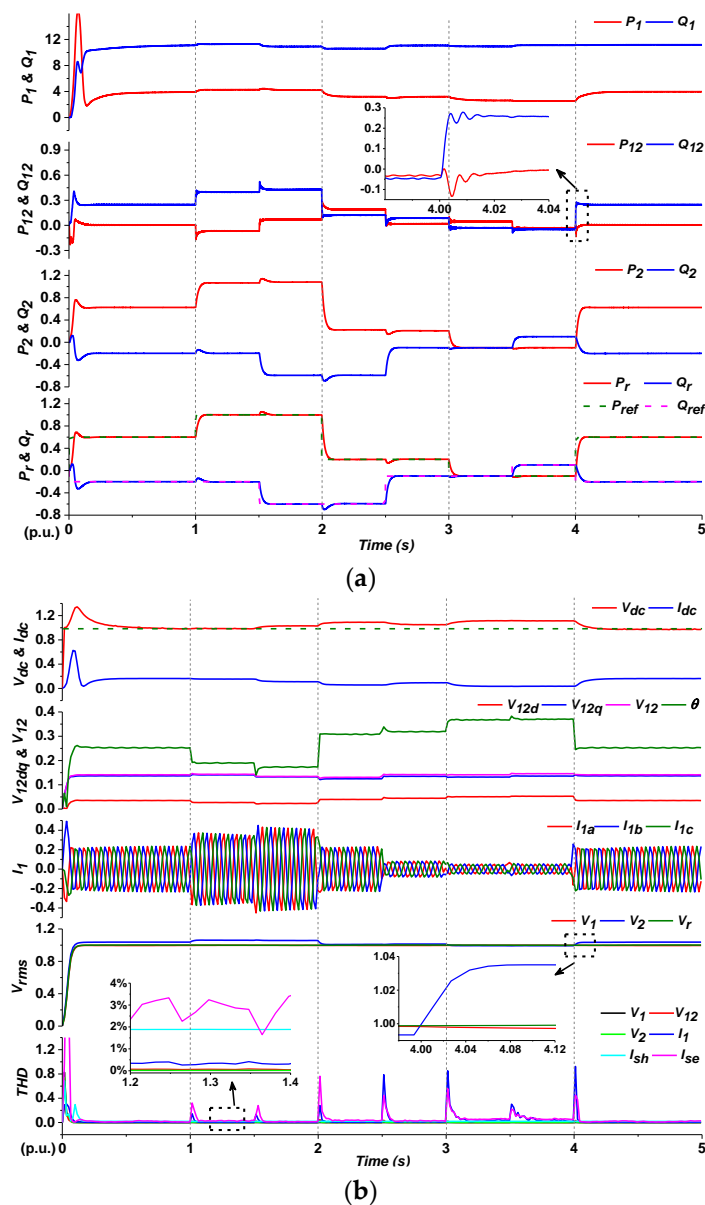
Figure 20. The simulation results of case 1. (**a**) The results of the power flow of each part; (**b**) The results of other important parameters.

5.2.2. Case 2: Steady-State Response Upon Variation of Voltage Magnitude and Phase Angle δ

In case 2, the voltage magnitude and phase angle difference between the two-ends sources are assumed to vary at the specified moment, and the simulation results are shown as Figure 21. First, it can be seen that the fluctuating ranges and decaying times of the power flow of each part turned out to be a little bigger and longer than those of case 1, the fluctuating ranges had increased to about 0.5 p.u., and the decaying times to the steady-state had prolonged to 300–400 ms. The results indicate that the variations of phase angle difference had a bigger impact on the power flow variation than the regulating of power flow references, but the performance had remained within the satisfactory ranges. Moreover, although the regulation efficiency of the series transformer v_{12} may had been more impacted, the damping out time of power flow oscillation had merely extended to 30ms-50ms, implying that the operation and function of MMC-based UPFC will hardly be influenced by phase angle variation.
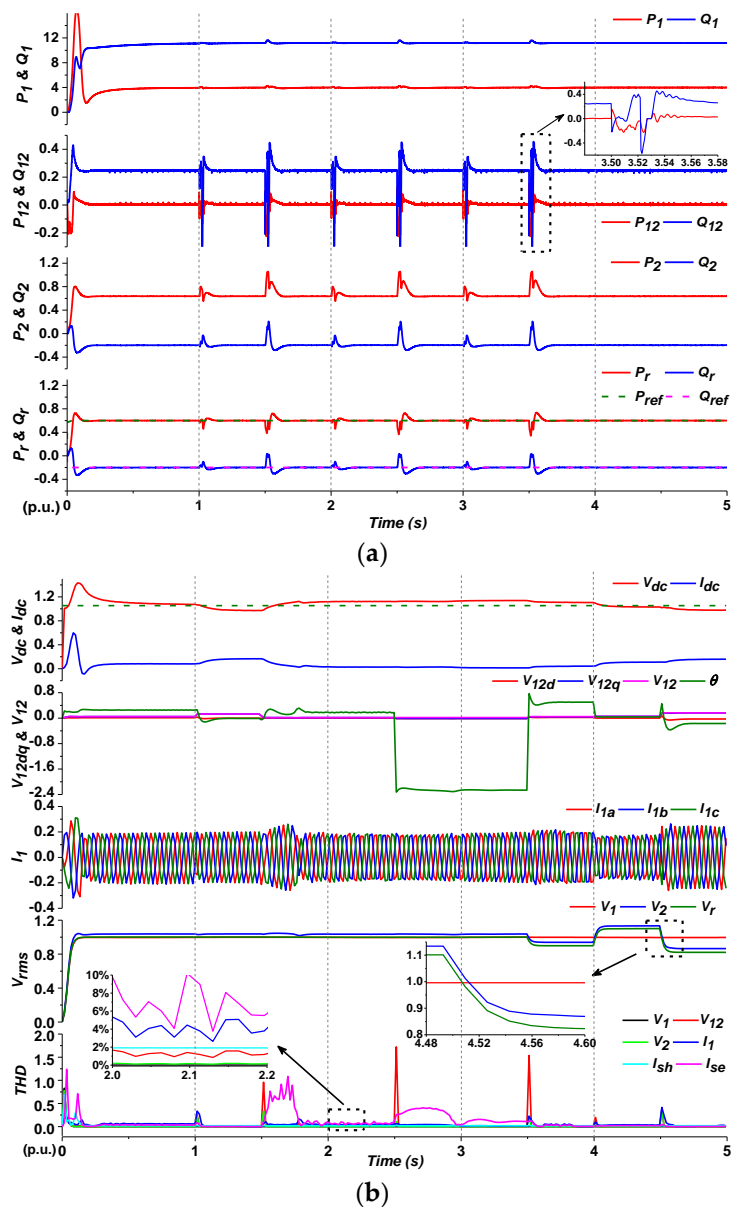
Figure 21. The simulation results of case 2. (**a**) The results of the power flow of each part; (**b**) The results of other important parameters.

It can be also seen that the back-to-back dc voltage and current had performed similarly to those of case 1, so as the magnitudes of V_1, V_2, V_r, and the components of v_{12}. Even under the worst condition of $V_r = 0.82$, $\delta = -\pi/2$, the measured voltage and current signals were still able to transit to the steady-state within tens to hundreds of milliseconds after fluctuations.

What should be noted is that the THD of several parameters had increased to some extent under steady-state, some of which had increased a little to 4%-10% due to the varying worse conditions, while the others also kept below 2%, indicating that the phase angle change had more impact on the power quality, but the influence is definitely within the satisfactory limits.

5.2.3. Case 3: Dynamic Response on Ground-faults at Different Positions, and Sudden Load Changes

In case 1 and case 2, we have analyzed the steady-state performance of the MMC-based UPFC. Finally, in this section, we assume to apply specified single and three-phase grounding faults at the initial point, the middle point, and the end point of the transmission line, also with the sudden load

change faults at the receiving end, to demonstrate the dynamic performance of MMC-based UPFC. The grounding faults are represented by F_1, F_2, F_3 in Figure 19, respectively, and the occurring moments of all the assumed faults were also listed as Table 4. The simulation results are displayed in Figure 22.
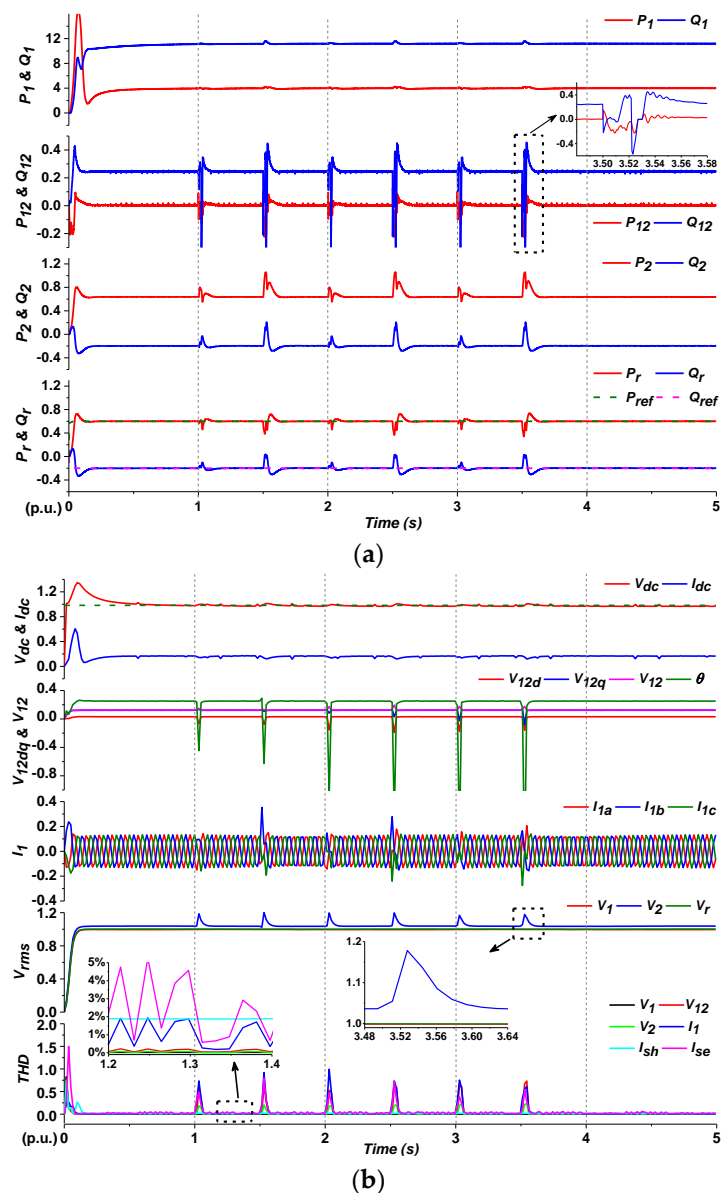
Figure 22. The simulation results of case 3. (**a**) The results of the power flow of each part; (**b**) The results of other important parameters.

It can be seen that on the one hand, the dynamic responses of the power flow of each part had presented little differences when the faults at different positions were applied, implying the positions of grounding faults had little influence on the dynamic response of the system. On the other hand, the fluctuating ranges of the power flow of each part at each fault position were almost within about 0.4 p.u., and the decaying times had merely extended to around 200ms under three-phase grounding faults which are a little worse than those of case 1, but better than those of case 2. In contrast, the performance of UPFC under single-phase grounding faults was similar to those of case 1. The results indicated that the three-phase grounding faults had impacted the system more intensely, but the dynamic performance was still satisfactory.

The exception was the dynamic responses of power flow v_{12} had deteriorated to some extents compared to those of both case 1 and case 3 no matter under single-phase or three- phase grounding faults. The fluctuating ranges had extended to 0.6 p.u. and decay time of oscillation had delayed to 50ms-80ms. We can also see the phase θ of v_{12} varied more sharply than the two former cases. The results reveal that although the dynamic response of UPFC may be influenced most by the grounding faults, the response speed, and precision were also enough excellent.

In addition, the faults of the sudden load change at the receiving end had presented almost no apparent impact on all the power flow through observation, indicating the regulation characteristics of MMC-based UPFC are tough and strong to the sudden load change at the receiving end.

As for the performance of other parameters, most of which had presented no much difference to those of two former cases. What should be noted is that the THD of several parameters still stayed within 5% under steady-state which were between those of case 1 and case 2, validating the satisfactory performance of MMC-based UPFC in dynamic response.

Until now, we have demonstrated that the MMC-based UPFC with the proposed feedforward coordination control strategy were able to achieve satisfactory accuracy, response speed, and stability both in the steady-state and dynamic response under three different cases, and validate the power flow principles proposed earlier in Section 3.

6. Conclusions

In this paper, we mainly established and analyzed the detailed power flow of a two-ends system embedded UPFC from different graphical viewpoints, then design a feedforward coordination control strategy to regulate UPFC, and finally verify the agreement of the proposed power flow principles and the efficiency of the control strategy by numerical simulation. Here, we can draw the following conclusions.

1. The graphical analyses of UPFC combining the plane and spatial viewpoints can be applied to the dispatchers with comprehensive power flow principles and qualitative regulation references of UPFC. The regulation of UPFC is mainly achieved through the series embedded voltage. There may exist more intense fluctuations and higher THD within the intersecting regions of real and reactive power. The maximal capacity of UPFC can provide enough reactive power support to maintain the system stable even under the worst condition.
2. In the proposed control strategy, there are two feedforward blocks introducing necessary compensating branches, related to the input reference of the inner-loops for both the shunt and series converter, respectively. They have achieved satisfactory accuracy, response speed, and stability in the complex and time domain through calculation and theoretical analyses.
3. In the simulation, the fluctuating ranges of power flow of each part are within 0.5 p.u., the decay times of oscillations are within 20–50 ms and the THD of most parts are within 3%–10% in steady-state response. Also, the above performance in the dynamic response are 0.6 p.u., 50–80 ms and 5%, respectively, verifying that the MMC-based UPFC can regulate the power flow of the system excellently both in the steady-state and dynamic state, and validating the agreement with the proposed power flow principles and the efficiency of the feedforward control strategy.

Appendix A

Table A1. Figures of characteristics performance of all the designed control components.

Components	Mag-Phase Characteristic Curves of Open-Loop	Log-Magnitude-Versus-Phase Plots	Time Domain Response to Three Exciting Sources
Current inner-loop of both converters			
Feedforward control related to i_{shd}			
Feedforward control related to i_{shq}			
Voltage Outer-loop of series converter			
Feedforward control related to v_{12d} **and** v_{12q}			

References

1. Hingorani, N.G.; Gyugyi, L. *Understanding FACTS: Concepts and Technology of Flexible AC Transmission Systems*, 1st ed.; Institute of Electrical and Electronics Engineers: New York, NY, USA, 1999; pp. 1–13.
2. Coates, D. FACTS: A transmission utility perspective. In Proceedings of the IEE Colloquium Flexible AC Transmission Systems—The FACTS, London, UK, 23 November 1998; pp. 1–7.
3. Gyugyi, L. Converter-based FACTS controllers. In Proceedings of the IEE Colloquium Flexible AC Transmission Systems—The FACTS, London, UK, 23 November 1998; pp. 1–11.
4. Johnson, B.K. Applications of FACTS 2011. In Proceedings of the IEEE/PES Power Systems Conference and Exposition, Phoenix, AZ, USA, 20–23 March 2011; pp. 1–2.
5. Paserba, J.J. How FACTS controllers benefit AC transmission systems-phases of power system studies. In Proceedings of the IEEE/PES Power Systems Conference and Exposition, Seattle, WA, USA, 15–18 March 2009; pp. 1–4.
6. Hingorani, N.G. FACTS technology and opportunities. In Proceedings of the IEE Colloquium on Flexible AC Transmission Systems (FACTS), London, UK, 12 January 1994; pp. 1–10.

7. Gyugyi, L. A unified power flow control concept for flexible AC transmission systems. In Proceedings of the International Conference on AC and DC Power Transmission, London, UK, 17–20 September 1992; pp. 19–26.

8. Rodriguez, J.; Lai, J.S.; Peng, F.Z. Multilevel Inverters: A survey of Topologies, Controls, and Applications. *IEEE Trans. Ind. Electron.* **2002**, *49*, 724–738. [CrossRef]

9. Hagiwara, M.; Akagi, H. Control and Experiment of Pulsewidth—Modulated Modular Mulitilevel Converters. *IEEE Trans. Power Electron.* **2009**, *24*, 1737–1746. [CrossRef]

10. Saeedifard, M.; Iravan, R. Dynamic performance of a modular multilevel back-to-back HVDC system. *IEEE Trans. Power Deliv.* **2010**, *25*, 2903–2912. [CrossRef]

11. Teeuwsen, S.P. Modeling the Trans Bay Cable Project as Voltage-Sourced Converter with Modular Multilevel Converter design. In Proceedings of the IEEE Power and Energy Society General Meeting, Detroit, MI, USA, 24–29 July 2011; pp. 1–8.

12. Li, P.; Lin, J.; Kong, X.; Wang, Y. Application of MMC-UPFC and its performance analyses in Nanjing Western Grid. In Proceedings of the IEEE PES Asia-Pacific Power and Energy Engineering Conference (APPEEC), Xi'an, China, 25–28 October 2016; pp. 2601–2605.

13. Li, P.; Wang, Y.; Feng, C.; Lin, J. Application of MMC-UPFC in the 500 kV power grid of Suzhou. *J. Eng.* **2017**, *13*, 2514–2518. [CrossRef]

14. Papic, I. Mathematical analyses of FACTS devices based on a voltage source converter Part 1: Mathematical models. *Electr. Power Syst. Res.* **2000**, *56*, 139–148. [CrossRef]

15. Vural, A.M.; Tumay, M. Steady state analysis of unified power flow controller: mathematical modeling and simulation studies. In Proceedings of the IEEE Bologna Power Tech Conference Proceedings, Bologna, Italy, 23–26 June 2003; pp. 1–6.

16. Zhang, N.; Liu, J.; Zhou, Q.; Hu, H.; Jing, C.; An, H. A review of different UPFC steady models in power flow algorithm. In Proceedings of the International Conference on Electric Utility Deregulation and Restructuring and Power Technologies, Changsha, China, 26–29 November 2015; pp. 2420–2424.

17. Pereira, M.; Zanetta, L.C. A current based model for load flow studies with UPFC. *IEEE Trans. Power Syst.* **2013**, *28*, 677–682. [CrossRef]

18. Huang, Z.; Ni, Y.; Shen, C.M.; Wu, F.F.; Chen, S.; Zhang, B. Application of Unified Power Flow Controller in Interconnected Power Systems—Modeling, Interface, Control Strategy, and Case Study. *IEEE Trans. Power Syst.* **2000**, *15*, 817–824. [CrossRef]

19. Haque, M.H.; Yam, C.M. A simple method of solving the controlled load flow problem of a power system in the presence of UPFC. *Electr. Power Syst. Res.* **2003**, *65*, 55–62. [CrossRef]

20. Lombard, X.; Therond, P.G. Control of Unified Power Flow Controller: comparison of methods on the basis of a detailed numerical model. *IEEE Trans. Power Syst.* **1997**, *12*, 824–830. [CrossRef]

21. Rahman, M.; Ahmed, M.; Gutman, R.; O'Keefe, R.J.; Nelson, R.J.; Bian, J. UPFC application on the AEP system: planning considerations. *IEEE Trans. Power Syst.* **1997**, *12*, 1695–1701. [CrossRef]

22. Fujita, H.; Watanabe, Y.; Akagi, H. Control and Analyses of a Unified Power Flow Controller. *IEEE Trans. Power Electr.* **1999**, *14*, 1021–1027. [CrossRef]

23. Martins, I.M.; Barros, J.D.; Silva, F.A. Design of cross-coupling free current mode controller for UPFC series converter. In Proceedings of the 11th International Conference on Optimization of Electrical and Electronic Equipment, Brasov, Romania, 22–24 May 2008; pp. 209–218.

24. Zhu, P.; Liu, L.; Liu, X.; Kang, Y.; Chen, J. Performance of a Decoupling Control Scheme for a Unified Power Flow Controller. In Proceedings of the 31st Annual Conference of IEEE Industrial Electronics Society, Raleigh, NC, USA, 6–10 November 2005; pp. 877–882.

25. Yam, C.M.; Haque, M.H. Dynamic Decoupled Compensator for UPFC Control. In Proceedings of the International Conference on Power System Technology, Kunming, China, 13–17 October 2002; pp. 1482–1487.

26. Mokhlis, H.; Nor, K.M. Implementation of UPFC model into Fast decoupled load flow. In Proceedings of the IEEE Region 10 Conference TENCON, Chiang Mai, Thailand, 22–24 November 2004; pp. 339–342.

27. Zhang, X.; Xu, P.; Zhang, C.; Ji, J.; Ding, M. Forward-feed decoupling based UPFC and converter system design. In Proceedings of the International Conference on Power System Technology, Kunming, China, 13–17 October 2002; pp. 2269–2274.

28. Dong, L.Y.; Zhang, L.; Crow, M.L. A New Control Strategy for the Unified Power Flow Controller. In Proceedings of the IEEE Power Engineering Society Winter Meeting, New York, NY, USA, 27–31 January 2002; pp. 562–566.

29.　Kannan, S.; Jayaram, S.; Salama, M.M. Real and Reactive Power Coordination for a Unified Power Flow Controller. *IEEE Trans. Power Syst.* **2004**, *19*, 1454–1461. [CrossRef]

30.　Monteiro, J.; Pinto, S.; Martin, A.D. A New Real Time Lyapunov Based Controller for Power Quality Improvement in Unified Power Flow Controllers Using Direct Matrix Converters. *Energies* **2017**, *10*, 779. [CrossRef]

31.　Song, P.; Xu, Z.; Dong, H.; Cai, H.; Xie, Z. Security-constrained line loss minimization in distribution systems with high penetration of renewable energy using UPFC. *J. Mod. Power Syst. Clean Energy* **2017**, *5*, 876–886. [CrossRef]

32.　Ahmad, S.; Albatsh, F.M.; Mekhilef, S.; Choudhury, F.; Hasan, M.M.; Nath, S.K. Implementation of Fuzzy Unified Power Flow Controller to Control Power Flow Dynamically in Transmission Line. In Proceedings of the International Conference on Advances in Electrical Engineering (ICAEE), Dhaka, Bangladesh, 17–19 December 2015; pp. 271–275.

33.　Nayeripour, M.; Narimani, M.R.; Niknam, T. Design of sliding mode controller for UPFC to improve power oscillation damping. *Appl. Soft Comput.* **2011**, *11*, 4766–4772. [CrossRef]

34.　Tu, Q.; Xu, Z.; Xu, L. Reduced switching—Frequency modulation and circulating current suppression for modular multilevel converters. *IEEE Trans. Power Deliv.* **2011**, *26*, 2009–2017.